Control of 3D tectonic inheritance on fold-and-thrust belts: insights from 3D numerical models and application to the Helvetic nappe system

Richard Spitz[1], Arthur Bauville[2], Jean-Luc Epard[1], Boris J.P. Kaus[3], Anton A. Popov[3], and Stefan M. Schmalholz[1]

[1]Institute of Earth Sciences, University of Lausanne, 1015 Lausanne, Switzerland
[2]Department of Mathematical Science and Advanced Technology, Japan Agency for Marin-Earth Science and Technology, 3173-25, Showa-machi, Kanazawa-ku Yokohama, Japan
[3]Institute of Geosciences, Johannes Gutenberg University Mainz, Mainz 55128, Germany

Correspondence: Richard Spitz (richard.spitz@unil.ch)

Abstract

We apply three-dimensional (3D) thermo-mechanical numerical simulations of the shortening of the upper crustal region of a passive margin to investigate the control of 3D laterally variable inherited structures on the fold-and-thrust belt evolution and associated nappe formation. We consider tectonic inheritance by applying an initial model configuration with horst and graben structures having laterally variable geometry and with sedimentary layers having different mechanical strength. We use a visco-plastic rheology with temperature dependent flow laws and a Drucker-Prager yield criterion. The models show the folding, detachment and horizontal displacement of sedimentary units, which resemble structures of fold and thrust nappes. The models further show the stacking of nappes. The detachment of nappe-like structures is controlled by the initial basement and sedimentary layer geometry. Significant horizontal transport is facilitated by weak sedimentary units below these nappes. The initial half-graben geometry has a strong impact on the basement and sediment deformation. Generally, deeper half-grabens generate thicker nappes and stronger deformation of the neighboring horst while shallower half-grabens generate thinner nappes and less deformation in the horst. Horizontally continuous strong sediment layers, which are not restricted to inital graben structures, cause detachment folding and not overthrusting. The amplitude of the detachment folds is controlled by the underlying graben geometry. A mechanically weaker basement favors the formation of fold nappes while stronger basement favors thrust sheets. The model configuration is motivated by applying the 3D model to the Helvetic nappe system of the Central Alps of France and Switzerland. Our model is able to reproduce several first-order structural features of this nappe system, namely (1) closure of a half-graben and associated formation of the Morcles and Doldenhorn nappes, (2) the overthrusting of a nappe resembling the Wildhorn and Glarus nappes and (3) the formation of a nappe pile resembling the Helvetic nappes resting above the Infrahelvetic complex. Furthermore, the finite strain pattern, temperature distribution and timing of the 3D model is in broad agreement with data from the Helvetic nappe system. Our model, hence, provides a

first-order 3D reconstruction of the tectonic evolution of the Helvetic nappe system based on thermo-mechanical deformation processes. Moreover, we apply only a standard visco-plastic rheology without additional strain softening mechanisms, which shows that such softening mechanisms are not essential to generate the first-order tectonic features of tectonic nappe systems.

1   Introduction

25   Fold-and-thrust belts are common in nature and typically associated with orogenic belts, such as the Himalayas or the European Alps. The structural interpretation of fold-and-thrust belts is based on the interaction between the crystalline basement and the overlying sedimentary cover. Two end-member deformation styles are commonly distinguished: thin-skinned deformation, without significant basement involvement, and thick-skinned deformation, with significant basement involvement (Rodgers, 1949; Pfiffner, 2006). Due to their importance for the fundamental understanding of mountain building processes and for

30   natural resources exploration, the formation of fold-and-thrust belts has been studied since several decades with field and modelling studies (e.g. Davis et al., 1983; Dahlen, 1984; Dahlen and Suppe, 1988; Beutner, 1977; Price and McClay, 1981; Gillcrist et al., 1987; Butler, 1989; Ramsay, 1989; Buchanan and Buchanan, 1995: Dunn et al., 1995; Mitra, 1997; Lacombe and Mouthereau, 2002; Wissing and Pfiffner, 2003; Simpson, 2011; Yamato et al., 2011; Ruh et al., 2012; Fernandez and Kaus, 2014; Bellahsen et al., 2012; Bauville and Schmalholz, 2015; Lacombe and Bellahsen, 2016; Bauville and Schmalholz, 2017).

35   However, the mechanical deformation processes controlling fold-and-thrust belt evolution are still incompletely understood. One challenge for understanding fold-and-thrust belt evolution is that the formation, spacing, orientation and time-sequence of thrusts, shear zones and folds are controlled by two different factors: First, the mechanical deformation behavior of rocks, which can be dominated either by brittle-frictional sliding or by ductile creep and can further be strongly affected by various mechanical softening mechanisms, such as frictional strain softening, reduction of effective friction by fluid overpressure,

40   grain size reduction with damage or thermal softening. Second, the geometrical configuration, such as half-graben structures or orientation of sedimentary layers, and variations in rock strength, for example between basement and cover or within the cover by alternation of strong, such as carbonates, and weak, such as shales, sediments. Therefore, a main challenge for understanding the thermo-mechanical evolution of fold-and-thrust belts is to determine whether the major thrusts and shear zones have been controlled by a particular rheological softening mechanism or by pre-existing geometrical and mechanical

45   heterogeneities, referred to here as tectonic inheritance. In nature, there is most likely a continuous transition between these two controlling factors.

   Many studies employing numerical models have been performed with a focus on the impact of different rheological models. Studies investigated the impact of brittle, brittle-ductile, visco-plastic and visco-elasto-plastic rheological models on fold-and-thrust belt evolution, and also studied, for example, the impact of fluid pressure and associated reduction of the effective friction

50   coefficient (e.g. Simpson, 2011; Ruh et al., 2014; Poulet et al., 2014; Bauville and Schmalholz, 2015; Granado and Ruh, 2019). Other numerical studies focused more on the impact of tectonic inheritance, in the form of mechanical heterogeneities, on fold-and-thrust belt evolution (Wissing and Pfiffner, 2003; Bauville and Schmalholz, 2017). To illustrate the two major control factors, namely rheology and tectonic inheritance, in a simple way, let us consider the deformation of a linear viscous material

under homogeneous pure shear. Adding a circular inclusion with a smaller viscosity to the viscous material will not generate a significant shear zone inside the linear viscous material for this deformation configuration. The only possibility to generate a shear zone in the viscous material is to add a softening mechanism, such as thermal softening (Jaquet et al., 2015; Kiss et al., 2019) or grain-size reduction with damage (Bercovici and Ricard, 2003; Austin et al., 2008). In contrast, if the linear viscous material is sheared over a non-planar interface, resembling a half-graben, then a shear zone can develop inside the linear viscous material even without any softening mechanism (Bauville and Schmalholz, 2017). Hence, strain localization can be caused by material softening and by mechanical heterogeneity.

The majority of numerical modeling studies uses two dimensional (2D) models, which were often able to produce results that are to first order comparable with geological reconstructions and cross-sections. However, it is well known that the style of fold-and-thrust belts can vary considerably along the strike of the belt (e.g. Hamilton, 1988; Mitra and Fisher, 1992; Mitra, 1997; Mouthereau et al., 2002; Fitz Diaz et al., 2011; Nemčok et al., 2013). Inherited, laterally varying pre-existing structures are important, for example, in the Alps where pre-Alpine laterally varying passive margin structure presumably exert a strong control on the deformation style (Pfiffner, 1993; Pfiffner et al., 2011). A recent study of the Iberian passive margin by Lymer et al. (2019) highlights the complex 3D architecture of such margins. Their results imply that fault systems disappear laterally or link together in lateral direction along the margin, consequently creating discontinuities and geometrical asymmetries. Therefore, it is important to consider the 3D inherited heterogeneities of passive margins when studying fold-and-thrust belts that resulted from the deformation of passive margins, as is the case for the Helvetic fault-and-thrust belt (Pfiffner et al., 2011).

Here, we apply a 3D thermo-mechanical numerical model to investigate the fundamental impacts of mechanical heterogeneities, representing graben structures and sedimentary layering, on the deformation style during fold-and-thrust belt formation. A particular aim is to apply our model results to the Helvetic nappe system in the Central Alps of France and Switzerland (see next section). We employ an initial model configuration that mimicks a simplified upper crustal region of a rifted margin and is composed of a basement and several sedimentary units. The passive margin contains a half-graben system that has a variable depth and width in the lateral direction. Moreover, we apply laboratory derived temperature dependent dislocation creep flow laws for all our model units and consider a brittle-frictional Drucker-Prager yield stress. We use a typical velocity boundary condition to simulate the large scale deformation conditions during tectonic wedge formation (Simpson, 2011; Ruh et al., 2014). In order to to focus on the large scale processes, we keep our model relatively simple and concentrate on the thermo-mechanical processes on the macroscale and the impact on kilometer-scale structures. Hence, we do not consider microscale processes such as grain size reduction involving secondary mineral phases and damage. Furthermore, our model does not include hydro-chemical coupling. Hence, we do not model processes such as fluid release and decarbonatization (Poulet et al., 2014).

The aims of our study are to: (1) understand the impact of lateral variations in half-graben geometry on the deformation style, (2) investigate the importance of the spatial distribution of a competent layer and half-graben geometry during fold-and-thrust belt formation and (3) discuss the application of our numerical models to the formation of the Helvetic nappe system.
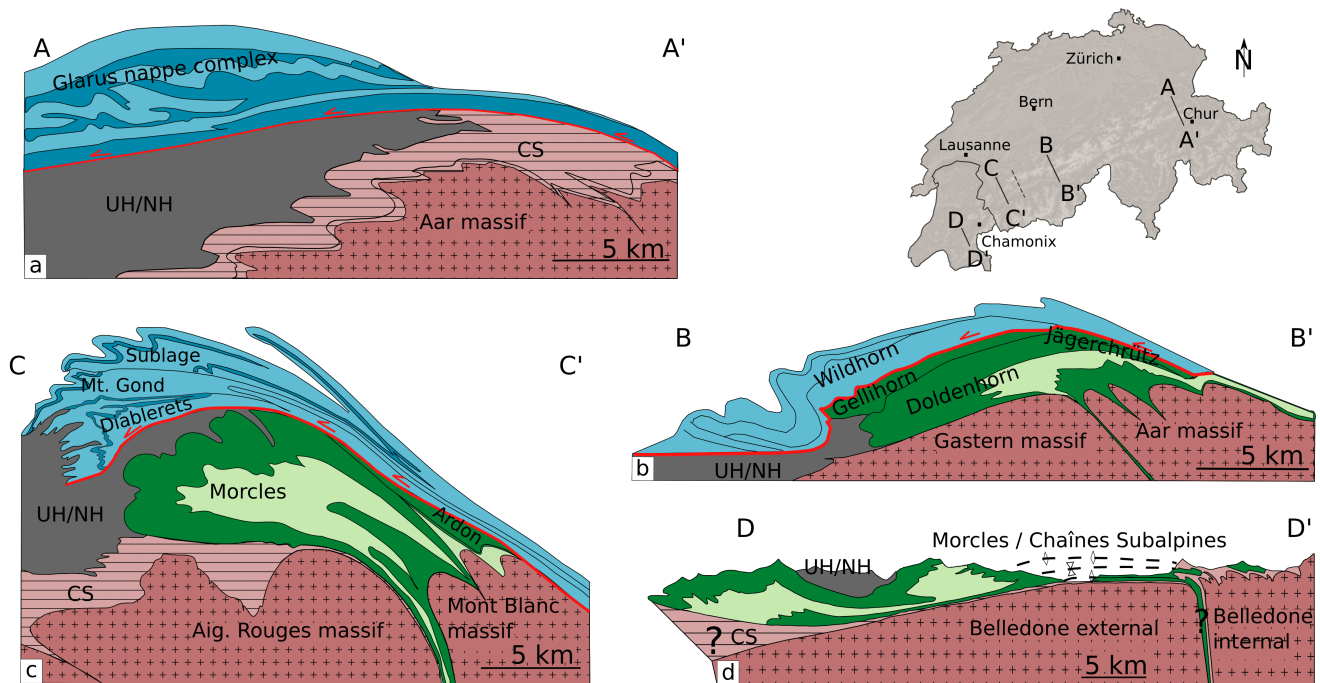
Figure 1. Simplified geological cross-sections along strike of the Helvetic nappe system. a) Glarus nappe complex (modified after Pfiffner, 2015). b) Doldenhorn nappe (modified after Kirschner et al., 1999). c) Morcles nappe (modified after Escher et al., 1993). d) Morcles nappe at the Belledonne massif (modified after Epard, 1990). UH/NH = Ultrahelvetics/North Helvetics. CS = Cover sediments.

2 Overview of the Helvetic Nappe system

The Helvetic nappe system is a fold-and-thrust belt complex that was formed during the Alpine orogeny when the European passive margin collided with the Adriatic margin (e.g. Trümpy et al., 1980; Pfiffner, 2015). The system consists of a pile of tectonics nappes, which mainly comprise Mesozoic and Cenozoic sediments derived from the former European continental margin (Masson et al., 1980; Ramsay, 1981; Pfiffner, 1993; Escher et al., 1993; Steck, 1999; Pfiffner et al., 2011). Commonly, the nappe system is subdivided in the structurally upper Helvetic nappes, considered mainly as allochtonous thrust nappes, and the structurally lower Infrahelvetic complex, which can involve par-authochtonous fold nappes (Pfiffner, 1993; Pfiffner et al., 2011) (Figure 1).

The onset of Alpine burial of the proto-nappe system is constrained by the last deposited sediments with ages of ca. 28 to 34 Ma (Kirschner et al., 1995; Nibourel et al., 2018). Peak metamorphic conditions in the Helvetic nappe system occurred between ca. 25 and 17 Ma, indicating the end of the main phase of nappe stacking (Kirschner et al., 1995; Nibourel et al., 2018). The main phase of nappe formation and stacking occurred presumably during a period of ca. 10 to 15 Ma (Masson et al., 1980; Milnes and Pfiffner, 1980; Burkhard, 1988; (Kirschner et al., 1995; Nibourel et al., 2018). Uplift and exhumation of the Helvetic nappe system occurred between ca. 20 Ma and today (Kirschner et al., 1995; Nibourel et al., 2018). We focus

here on the main phase of nappe formation and stacking and do not consider the subsequent uplift and exhumation of the Helvetic nappe system.

The Helvetic nappe system exhibits a wide range of nappe geometries, including two commonly considered end-member nappe styles, namely fold nappes and thrust nappes, or thrust sheets (Termier, 1906; Epard and Escher, 1996). Fold nappes are recumbent folds with fold amplitudes of several kilometers and with a stratigraphic inversion in a prominent overturned limb. Thrust nappes are coherent allochtohonous rock sheets that are displaced along a basal shear zone and lack a prominent overturned limb.

We consider here four simplified geological sections across the Helvetic nappe system in the Central Alps of France and Switzerland and focus on several prominent nappes within these sections (Figure 1). The first order tectonic features of these four cross sections and the associated nappes will be compared with our 3D modelling results.

The first section includes the Glarus nappe complex of eastern Switzerland (Figure 1a). Geological reconstructions suggest a displacement of approximately 50 km from its original location along a thin basal thrust zone that is composed of Mesozoic sediments (e.g. Pfiffner, 2015). Studies suggest that the Glarus basal thrust originates inside Carboniferous strata allowing for the transport of the Glarus nappe consisting of Permian Verrucano units at its base (e.g. Schmid, 1975; Pfiffner, 1993; Pfiffner, 2015). Observations on the thrust zone suggest earlier viscous dominated deformation followed by dominantly brittle deformation (Herwegh et al., 2008). A number of studies investigated the complex deformation behavior of the thrust zone and suggest the involvement of pressurized fluids that resulted in hydro-fracture networks and the reduction of friction at the base (e.g. Burkhard et al., 1992; Badertscher and Burkhard, 2000; Badertscher et al., 2002; Herwegh et al., 2008; Hürzeler and Abart, 2008). Recently, Poulet et al., 2014 suggest a superposition of viscous and brittle deformation mechanisms due to ductile shear heating resulting in decarbonatization and the release of overpressurized fluids causing brittle fracturing.

The second section includes the Doldenhorn fold nappe, belonging to the Infrahelvetic complex, which has been over-thrusted by the Wildhorn nappe, belonging to the Helvetic nappes (Figure 1b). The Doldenhorn nappe consists of Mesozoic and Cenozoic parautochthonous sediments that have been squeezed and sheared out of a pre-Alpine half-graben, referred to here as North Helvetic basin (Figure 2). The term North Helvetic basin refers here to a Jurassic extensional basin restricted to the Western region of the Helvetic nappe system and should not be confused with the Tertiary North Helvetic Flysch basin that is part of the North Alpine foreland basin. The Doldenhorn nappe is derived from the inversion of the North Helvetic basin which is restricted to the area west and south of the Aar massif. The Gellihorn and Jägerchrütz nappes are minor nappes and their sediments are considered as deposits on a basement high, likely a horst, which seperated the half-graben including the Doldenhorn sediments from the more distal marginal basin, referred to here as Helvetic basin, on which the Wildhorn sediments have been deposited (Masson et al., 1980) (Figure 2). The Doldenhorn nappe roots in the Aar basement massif. Studies indicate metamorphic peak temperatures in the Doldenhorn nappe of up to 380°C (Herwegh and Pfiffner, 2005; Ebert et al., 2007a). These temperatures allowed for ductile deformation and folding of the Doldenhorn nappe during nappe formation. Colder temperatures around ca. 250 °C in the structurally higher Wildhorn nappe were likely responsible for a deformation style resembling more a thrust nappe.

The third section includes the Morcles fold nappe (Figure 1c) belonging to the Infrahelvetic complex. It is overlain by a major thrust nappe, which is termed in this region the Wildhorn super-nappe (Steck, 1999). The term super-nappe is used, because the nappe can be subdivided, from bottom to top, into the Diablerets, Mont-Gond and Sublage nappes. Similarly to the Doldenhorn nappe, the Morcles nappe is considered as the result of the closure of the North Helvetic basin and the subsequent extrusion of sediments during compressional Alpine tectonics (e.g. Ramsay, 1981; Pfiffner, 1993). This North Helvetic basin comprised kilometer thick sequences of shale-rich units and competent carbonate units. The strongly thinned and overturned limb is in contact with the crystalline Aiguilles-Rouges massif below and its autochthoneous sediments. Between the Morcles and Wildhorn nappe is a minor sedimentary nappe, the Ardon nappe, which is considered as originating from the horst region, from a similar paleogeographic position as the Jägerchrütz nappe (Figure 2). Estimates of metamorphic peak temperatures range between $250°C$ and $380°C$ and therefore support a dominantly ductile deformation regime (Leloup et al., 2005; Boutoux et al., 2016). Furthermore, the deformation of the Morcles nappe is constrained by finite strain measurements. The data highlights a pattern of increasing strain from the front of the nappe towards the root zone and also from the top to the bottom. Strain ellipses show X/Y ratios > 400 at the contact between the overturned limb and the basement-cover (Ramsay and Huber, 1987; Casey and Dietrich, 1997). Microstructural observations of the basal mylonitic shear zone in the overturned limb of the fold nappe indicate ductile creep in the calcite-rich lithologies (Austin et al., 2008). The Wildhorn super-nappe, as a whole, resembles more a thrust sheet but exhibits significant internal deformation. For example, the Diablerets nappe is separated from the Mont Gond nappe by an isoclinal fold indicating significant ductile deformation inside the super-nappe.

Due to the structural Rawil depression, there is no continuous outcrop from the Doldenhorn towards the Morcle nappe. However, several geological reconstructions suggest, that the Doldenhorn and Morcles nappes originate from the same, lateral continuous North Helvetic basin and that the Wildhorn nappe and super-nappe result from the same laterally continuous Helvetic basin of the Mesozoic passive European margin (Burkhard, 1988; Epard, 1990). The North Helvetic basin is considered absent in the eastern region of the Helvetic nappe system, which explains the absence of significant recumbent fold nappes in the Infrahelvetic complex below the Glarus thrust. To first order, the Doldenhorn nappe is structurally similar to the Morcles nappe in that both nappes exhibit long inverted limbs, which are absent in the Glarus nappe complex.

The fourth section (Figure 1d) includes the Morcles nappe and the Chaînes Subalpines and is located in the French Alps. There are different interpretations concerning the tectonic relationship between the Morcles nappe and the Chaînes Subalpines in this region (Epard (1990); Pfiffner et al., 2011). Here, we follow the interpretations of Epard (1990) and Collet (1943) who consider this region of the Chaînes Subalpines as belonging to the same tectonic unit as the Morcles nappe. In other words, we assume that in the considered region the Chaînes Subalpines and Morcles nappe derived from the North Helvetic basin (Figure 2). In this section, no Helvetic nappes are outcropping. In contrast to the Morcles fold nappe in the third section, the nappe is here not a fold nappe but rather a thrust nappe (cp. Figure 1c and 1d, respectively), because there is no prominent overturned limb.

Some studies suggested mechanical explanations for the variation in nappe style within the Helvetic nappe system. The formation of fold nappes in the Southwestern part of Switzerland and the lack of such fold nappes in the Northeastern part is explained by lateral variations of the mechanical stratigraphy, that is the alteration of mechanically strong, such as carbonates,

and weak, such as shales, sedimentray units (Pfiffner, 1993; Pfiffner et al., 2011). Different thickness ratios, n, of weak to strong sedimentary units cause a different mechanical response during shortening. Low ratios $n < 0.5$ favor imbricate thrusting and harmonic folding while higher ratios of n favor fold nappes and detachment folding (Pfiffner, 1993). This impact of thickness ratios on deformation style, which was derived by field observations, is also supported by 2D numerical simulations (Jaquet et al., 2014). Moreover, Von Tscharner et al. (2016) quantified, with 3D numerical models of viscous deformation, the impact of laterally varying half-graben depth on the folding of sedimentary layers in the half-graben. Their 3D model results also confirm that laterally varying sediment thickness has a strong impact on fold amplification and nappe formation. However, their models do not generate thrust nappes and also not the stacking of nappes, as observed in the Helvetic nappe system. A comparison of observed finite strain gradients across the Morcles fold nappe with finite strain gradients resulting from a theoretical thermo-mechanical shear zone model utilizing calcite flow laws suggests that the Morcles fold nappe was generated by heterogeneous shearing during Alpine shortening (Bauville and Schmalholz, 2013), as was already suggested by kinematic models (Ramsay et al., 1983; Dietrich and Casey, 1989; Casey and Dietrich, 1997).

3   Methods

3.1   Numerical method

We apply the concept of continuum mechanics to describe the deformation of rocks with a system of partial differential equations (e.g. Mase, 1970). To solve the resulting system of equations numerically, we apply the 3D thermo-mechanical parallel code LaMEM (Kaus et al., 2016; https://bitbucket.org/bkaus/lamem) for our simulations. The equations describing the conservation of mass, linear momentum and energy are:

$$\frac{\partial v_i}{\partial x_i} = 0 \tag{1}$$

$$-\frac{\partial P}{\partial x_i} + \frac{\partial \tau_{ij}}{\partial x_j} = \rho g_i \tag{2}$$

$$\rho C_p \frac{\partial T}{\partial t} = \frac{\partial}{\partial x_i} \left(\lambda \frac{\partial T}{\partial x_i} \right) + H_R + H_S \tag{3}$$

where x_i (i = 1,2,3) refers to Cartesian coordinates in the three spatial directions (i=1 indicates x-direction, i=2 y-direction and i=3 z-direction), v_i are the components of the velocity vector, P is pressure (negative mean stress), $\tau_{ij} = \sigma_{ij} + P\delta_{ij}$ are components of the deviatoric Cauchy stress tensor (with δ_{ij} being the Kronecker delta), ρ is density, $g_i = [0\ 0\ g]$ the gravity acceleration vector with g being the gravitational acceleration, C_p is the specific heat, T the temperature and λ the thermal conductivity. The source term H_R refers to the radiogenic heat production and $H_S = \tau_{ij}\dot{\varepsilon}_{ij}$ for shear heating. The components of the deviatoric strain rate tensor $\dot{\varepsilon}_{ij}$ are defined by the visco-plastic constitutive equations:

$$\dot{\varepsilon}_{ij} = \dot{\varepsilon}_{ij}^{vs} + \dot{\varepsilon}_{ij}^{pl} = \frac{\tau_{ij}}{2\eta_{eff}} + \dot{\varepsilon}_{II}^{pl} \frac{\tau_{ij}}{\tau_{II}} \tag{4}$$

where $\dot{\varepsilon}_{ij}^{vs}$ is the viscous strain rate tensor, $\dot{\varepsilon}_{ij}^{pl}$ is the plastic strain rate tensor, η_{eff} is the effective viscosity, τ_{ij} are components of the deviatoric stress tensor and $\tau_{II} = (\frac{1}{2}\tau_{ij}\tau_{ij})^{\frac{1}{2}}$ is the square root of the second invariant of the deviatoric stress tensor.
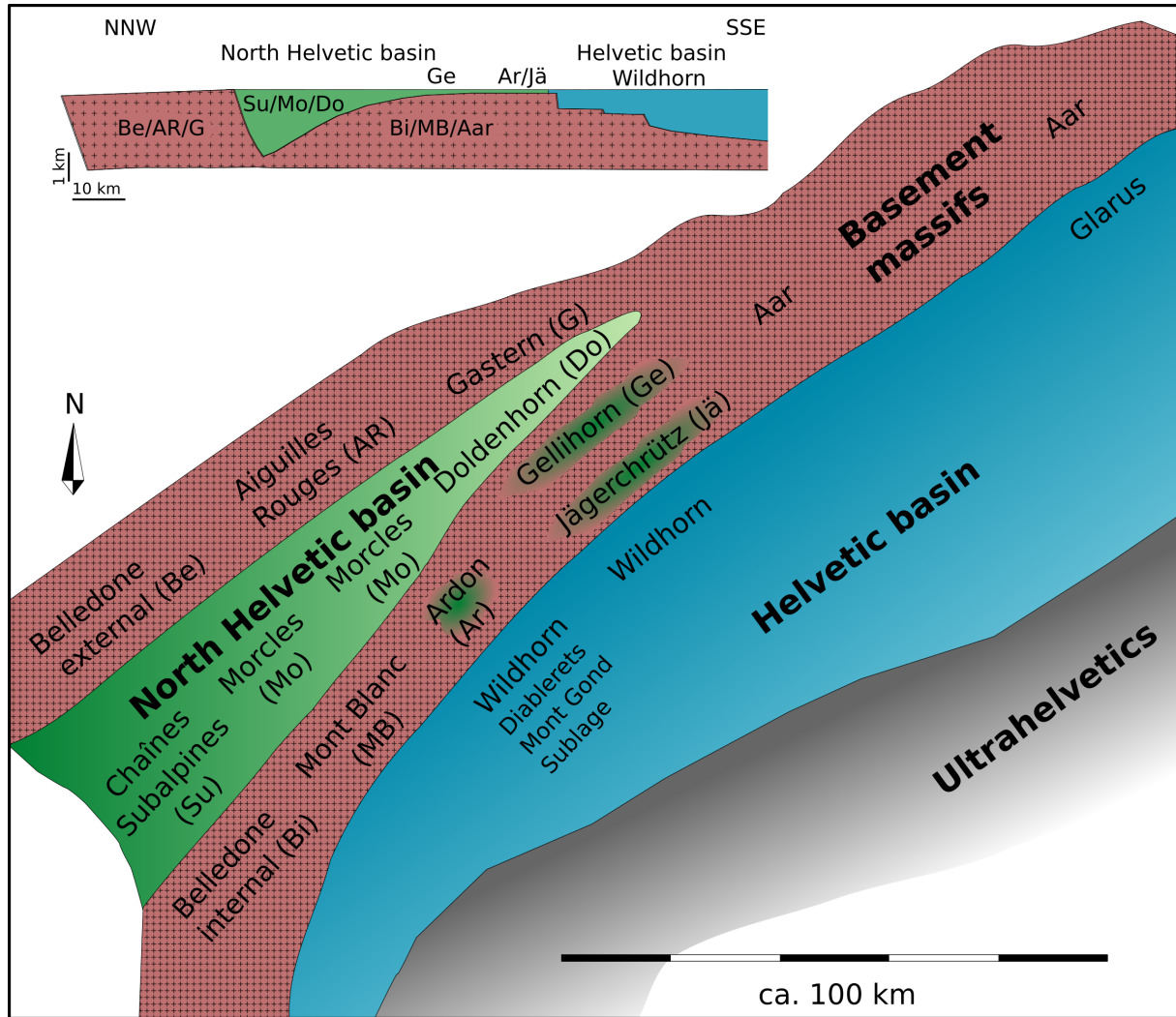
Figure 2. Simplified paleogeographic map of the lower cretaceous showing the assumed distribution of the basement massifs and sedimentary units forming the discussed tectonic nappes of the Helvetic nappe system (modified after Epard, 1990 and Pfiffner, 2015). The cross section on the top left represents a section through the SW region across the Helvetic nappe system (modified after Jaquet et al., 2018).

The temperature dependent viscosity η_{eff} for the considered dislocation creep is:

$$\eta_{eff} = \frac{1}{2} \left(B_n\right)^{-\frac{1}{n}} \left(\dot{\varepsilon}_{II}\right)^{\frac{1}{n}-1} exp\left(\frac{E_n}{nRT}\right)$$ (5)

where n is the stress exponent, $\dot{\varepsilon}_{II} = (\frac{1}{2}\dot{\varepsilon}_{ij}\dot{\varepsilon}_{ij})^{\frac{1}{2}}$ the square root of the second invariant of the strain rate tensor, B_n the creep constant, E_n the activation energy and R the universal gas constant. The components of the plastic strain rate tensor $\dot{\varepsilon}_{ij}^{pl}$ are determined by enforcing the Drucker-Prager yield criterion given by:
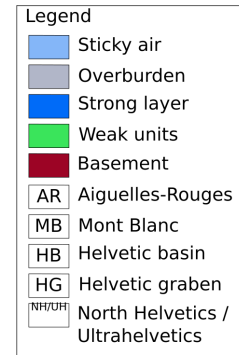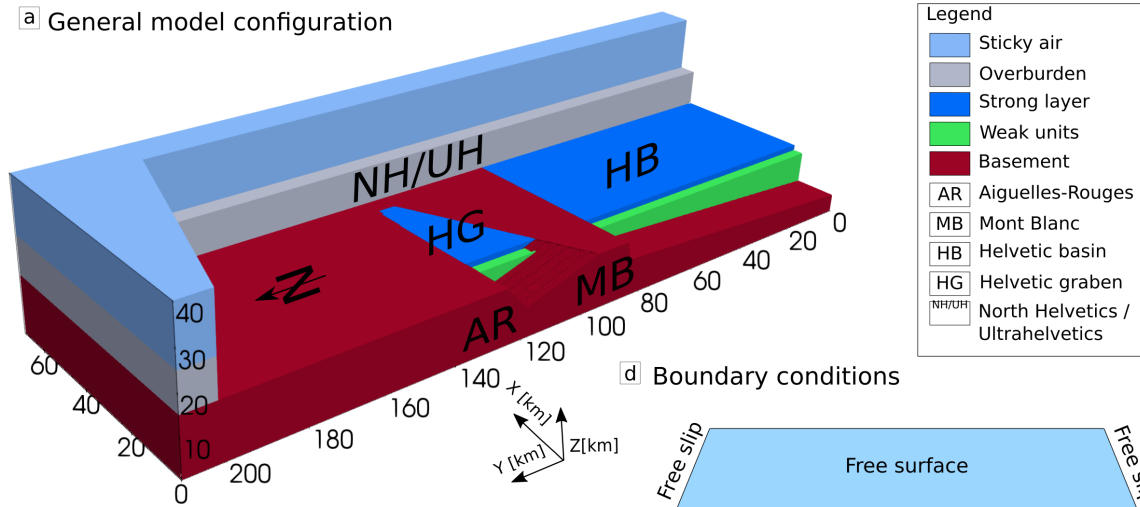
$$\tau_{II} \leq \tau_Y = \sin(\phi)P + \cos(\phi)C$$ (6)

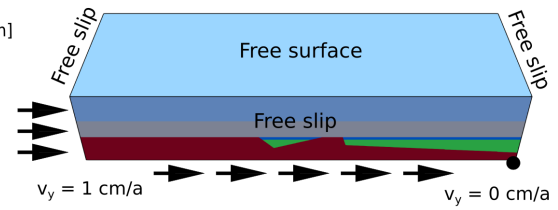Here, τ_Y is the yield stress, ϕ the friction angle and C the cohesion.

We do not consider erosion in our model, mainly because the main phase of basement uplift and exhumation started during the end of the main nappe forming phase, after ca. 20 Ma, and because our models do not generate significant lateral topographic variations (see results section).

The system of equations is discretized with a staggered grid finite difference approach and solved with LaMEM. Material properties are advected employing a marker-and-cell method. In order to maintain computational stability for large time steps we employ a stabilized free surface boundary condition. For detailed information on the LaMEM code see Kaus et al. (2016) and the documentation on the official website (https://bitbucket.org/bkaus/lamem).
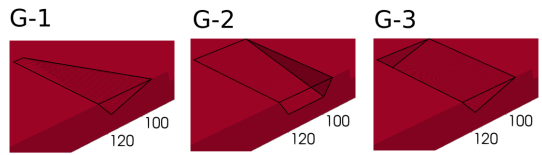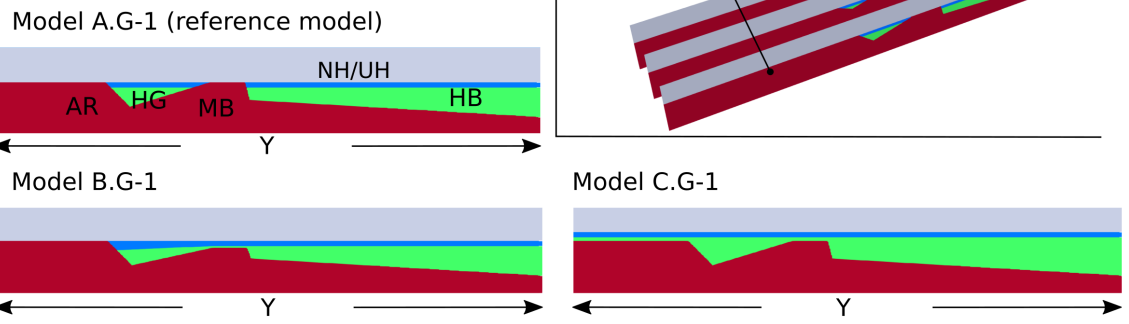
a General model configuration

Legend
- Sticky air
- Overburden
- Strong layer
- Weak units
- Basement
- AR Aiguelles-Rouges
- MB Mont Blanc
- HB Helvetic basin
- HG Helvetic graben
- NH/UH North Helvetics / Ultrahelvetics

NH/UH
HB
HG
AR MB

X [km]
Y [km] Z[km]

b Graben variations for model A

G-1   G-2   G-3

c Selected side view (X = 0 km)

Model A.G-1 (reference model)

NH/UH
AR HG MB HB
Y

Model B.G-1

Y

d Boundary conditions

Free slip   Free slip
Free surface
Free slip
$v_y = 1$ cm/a $v_y = 0$ cm/a

e Model evaluation by X-slices:

X

Model C.G-1

Y
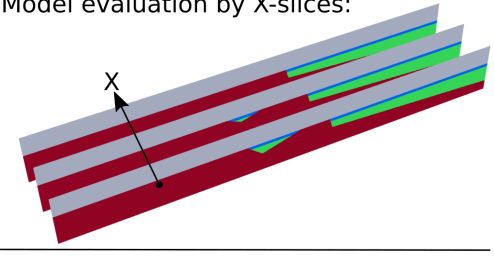
f Graphical overlay of passive marker lines used for numerical cross-sections

Model A.G-1 (reference model)

100
200
300
400
10 km

Model B.G-1

100
200
300
400
10 km
Y

10
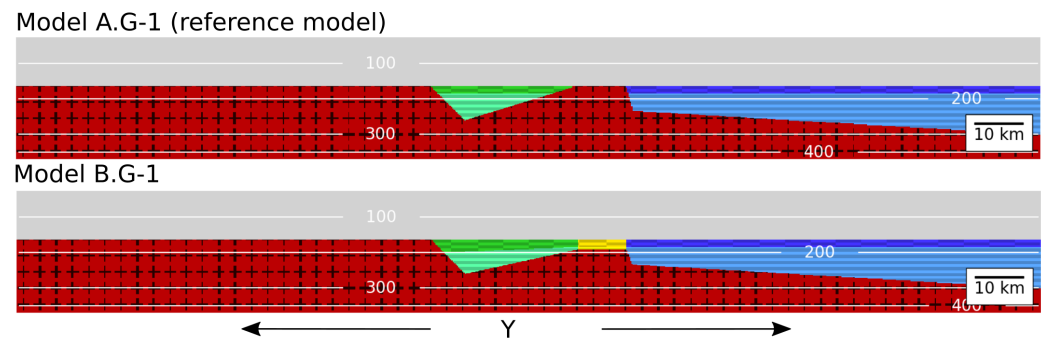
Figure 3. a) 3D geometry of our reference model configuration using a laterally disappearing half-graben, and highlighting the distribution of our numerical phases and their material properties. Here, the color *green* refers to weak materials and *dark blue* to strong materials. The configuration is based on the paleogeographic reconstructions as indicated by the abbreviations on the model: AR = Aiguilles Rouges massif, MB = Mont Blanc massif, HB = Helvetic Basin, NH/UH = North Helvetic flysch and Ultrahelvetic units, HG = North Helvetic graben. b) Display of our three different half-graben systems used as initial setup. c) Cross-sectional view at X = 0 km for three models utilizing half-graben G-1 in combination with three different stratigraphic distributions. d) Sketch displaying our boundary conditions. e) 3 cross-sectional slices along X-direction to explain our model evaluation. f) Subfigure highlighting our passive marker overlay which is used to distinguish the different structural units HG (*green*) and HB (*blue*) from each other. Temperature isotherms are shown in [$^{\circ}C$].

3.2 Model configuration

The model configuration (Figure 3a) has a lateral width of X = 70 km, a length of Y = 210 km and height of Z = 40 km. Our numerical resolution for most simulations is $128 \times 256 \times 128$ (X × Y × Z) grid points with a mesh refinement in Z-direction using 96 grid points between Z = 8 and 32 km and 16 grid points each for Z < 8 km and Z > 32 km. Our model consists of five units which are, from top to bottom: a sticky air, a cover, a strong layer, a weak unit and a basement unit. Each unit has distinctive mechanical properties, such as for example, a flow law, friction angle, or cohesion that corresponds to natural materials. In addition to the standard parameters of the flow laws we add a pre-factor f to the creep constant B_n to facilitate a brittle-ductile transition zone at a depth of $8-10$ km. The details of the mechanical properties for each unit are listed in Table 1. The initial model geometry is based on a simplified and idealized cross-section of the European crustal continental passive margin. The basement constitutes the bottom of the model domain and has a maximum height of 15 km. It involves a half-graben (HG) that is separated by a horst from a larger distal basin (HB) to the right (Figure 3b). HG represents the half-graben region in which the sediments of the Morcles and Doldenhorn nappes have been deposited, HB represents the Helvetic Basin in which the sediments of the Wildhorn nappe have been deposited and the horst between HG and HB represents the domain on which the sediments of the Ardon and Gellihorn nappes have been deposited (Fig. 2). In the reference configuration HG is becoming shallower and finally disappears towards the NE-direction (positive X-direction; Figure 3a). The half-graben, between 110 km > Y > 90 km, is subjected to different geometries in our different model configurations with respect to its lateral extend (X-direction). The total dimensions of the graben system are fixed with a maximum depth of 7 km, a length of 25 km (Y-direction) and a width of 50 km (X-direction). In contrast, the geometry of the distal basin (Y < 90 km) is constant and has no variations in the X-direction for all model configurations. Both half-graben and basin are filled with a weak unit, mimicking shale-rich sediments, that is overlain by a strong layer with a thickness of 1.5 km, mimicking strong carbonates. Additionally, we apply a 10 km thick sediment cover, mimicking the North Helvetic Flysch and Ultrahelvetic units. We assume that these cover unit have been thrust on top of the proto-Helvetic nappe system before the onset of nappe formation. Finally, we use a low density, low viscous sticky air unit ($\eta = 10^{19}\ Pa.s^{-1}$, $\rho = 1\ kg.m^{-3}$) on top to simulate a free surface boundary condition.

In order to investigate the impact of the geometry of HG on the structural evolution of our model we use two different series of simulations. In the first one, we vary the geometry of HG in lateral direction using three different geometries (Figure 3b),

namely G-1 to G-3. Here, we also define our reference model A.G-1. It compromises HG, G-1, that linearly shallows and narrows out in lateral X-direction. The next configuration, G-2, is HG without lateral geometrical variations, which is bounded by a 90° wall to the adjacent basement. Our third configuration, G-3, is HG being a full graben that shallows out in lateral direction while the length in Y-direction is constant.

In the second series (Figure 3c) we employ the same HG as in the reference configuration, G-1, but modify the spatial connection between the strong layer and the underlying basement. In model B.G-1 we decrease the height of the horst in such a way that the strong layer and a part of the weak unit rests on the top of the horst. Additionally, we also thicken the left part of the strong layer which is connected to the basement in a wedge like shape (Figure 3c). In the last model, C.G-1, we extend the strong layer to the left of the HG (Figure 3c). For C.G-1, the layer is not connected with the basement, but underlain by an additional 0.5 km thick layer of weak units (Figure 3c).

To test the impact of the vertical strength distribution in the basement, we performed an additional simulations, D.G-1, with the same configuration as the reference model, A.G-1, but we cut-off the deviatoric stresses in the basement at 40 MPa. Numerically, this is done by setting the cohesion in the basement to 40 MPa and setting the friction angle to zero. Such yield criterion corresponds essential to a pressure-insensitive von Mises yield strength and mimics a semi-brittle deformation, or a low temperature plasticity.

We apply free slip boundary conditions on all sides of the model except on the top where we model a free surface boundary condition with the sticky air method (Figure 3d). In order to mimic the kinematic conditions during tectonic wedge formation, we apply a constant velocity boundary condition on the bottom face and the left XZ-face of our model (Figure 3d). We induce bulk shortening of the model by moving the left boundary and the bottom boundary in positive Y-direction with a constant velocity of $v_y = 1\,cm/yr$. This boundary condition is similar to typical sandbox analogue models of accretionary wedge formation. The bulk shortening strain rate $\dot{\varepsilon}_{bg}$ is recalculated from the velocity boundary condition for every time step. The shortening of the model in Y-direction is balanced by an elongation in Z-direction, with no changes of the width in X-direction.

We use a linear, vertical temperature gradient of $16.6°C$/km with a fixed temperature of $20°C$ at the surface and $435°C$ at the bottom of the model. Further, we do not model surface erosion.

Furthermore, we use passive marker lines and patterns to improve the visualization of 2D cross-sections of our 3D model (Figure 3f). Also, we slightly change the color scheme to highlight the two major basement structures HG and HB, together with the sediments on top of the basement horst (*yellow*). The darker colors inside the HG and HB indicate the strong layer while the lighter colors correspond to the weak units. The layering and patterns are passively advected with the numerical velocity field. Hence, they do not influence the material properties and deformation and are simply there for visualization purposes.

12

| Model unit	ρ [$kg.m^{-3}$]	**Rheology**	f	A[$Pa^{-n}.s^{-1}$]	n	Q [$J.mol^{-1}$]	λ[$W.m^1K^{-1}$]	ϕ [°]	C [MPa]
Cover	2750	Calcite[1]	0.1	1.58×10^{-25}	4.2	4.45×10^5	2.0	30	1
Strong layer	2750	Calcite[1]	1.0	1.58×10^{-25}	4.2	4.45×10^5	2.5	30	1
Weak units	2750	Mica[2]	1.0	1×10^{-138}	18.0	5.10×10^5	2.5	5	1
Basement	2800	Granite[3]	1.0	3.16×10^{-26}	3.3	1.87×10^5	3.0	30	10

Table 1. Table listing the material properties of our model units for most models, where ρ is the density, A is the pre-exponential factor, f is custom pre-factor, n is the power-law exponent, Q is the activation energy, λ is the thermal conductivity, ϕ is the friction angle, and C is the cohesion. Some additional parameters are constant: Here the thermal expansion coefficient $\alpha = 3 \times 10^{-5}\ K^{-1}$, the heat capacity $C_p = 1050\ J.K^{-1}$ and the radiogenic heat production $Q_r = 10^{-6}\ W.m^{-3}$. We use following creep flow laws: [1]Schmid et al. (1977),[2]Hansen et al. (1983),[3]Kronenberg et al. (1990).

4 Results

4.1 3D model evolution

We first provide an overview of the general model evolution of all six performed 3D simulations. Figure 4 shows the structural evolution for three different bulk shortening for each model configuration. All models, except model C.G-1 (Figure 3c), show the formation of nappe-type structures in the strong layers and stacking of the strong layer from HB on top of the strong layer of HG. Model C.G-1 does not generate any nappe-like structure or overthrusting, but generates detachment folds.

In the first stage of our reference model A.G-1 (Figure 4a) the strong layer of HB is detached from the horst by the formation of a shear zone. Both the strong layer and the weak units below are thrusted on top of the horst culminating in a horizontal displacement of about 10 km. Our model generated a structure resembling a thrust sheet or thrust nappe. The HB experiences closure. In the region of HB, the weak sediments and the basement are thickened with ongoing bulk shortening. Initially, the basement experiences an uplift at the right boundary due to the imposed velocity discontinuity. The basement uplift increases the topography at the right boundary of the model (i.e. the backstop). The HG shows minor signs of deformation at 23%. The strong layer is partially sheared and squeezed out in front of HG. Additionally, we observe a slight depression of the strong layer in the rear of HG. In the next shortening stage, (Figure 4b) the closure and inversion of HG is in progress. The strong layer has been squeezed out of HG. The horizontal displacement of the strong layer of HG decreases in positive X-direction associated with decreasing depth of HG. Furthermore, the thrust nappe from HB has advanced on top of HG and the horst exhibits a dome-like shape. At 47 % bulk shortening (Figure 4c), the half-graben is almost completely closed resulting in the formation of a elongated cusp dipping towards the backstop. The infill of HG has been extruded and compromises a nappe that is overthrust by a nappe from HB. The front of the nappe from HB is essentially straight along the lateral, X-direction, indicating that the displacement of the nappe is essentially unaffected by the formation of the nappe below, whose front varies significantly along the X-direction. We only observe a slightly higher topography above the nappe from HG, causing a slight tilting of the nappe from HB towards the positive X-direction.
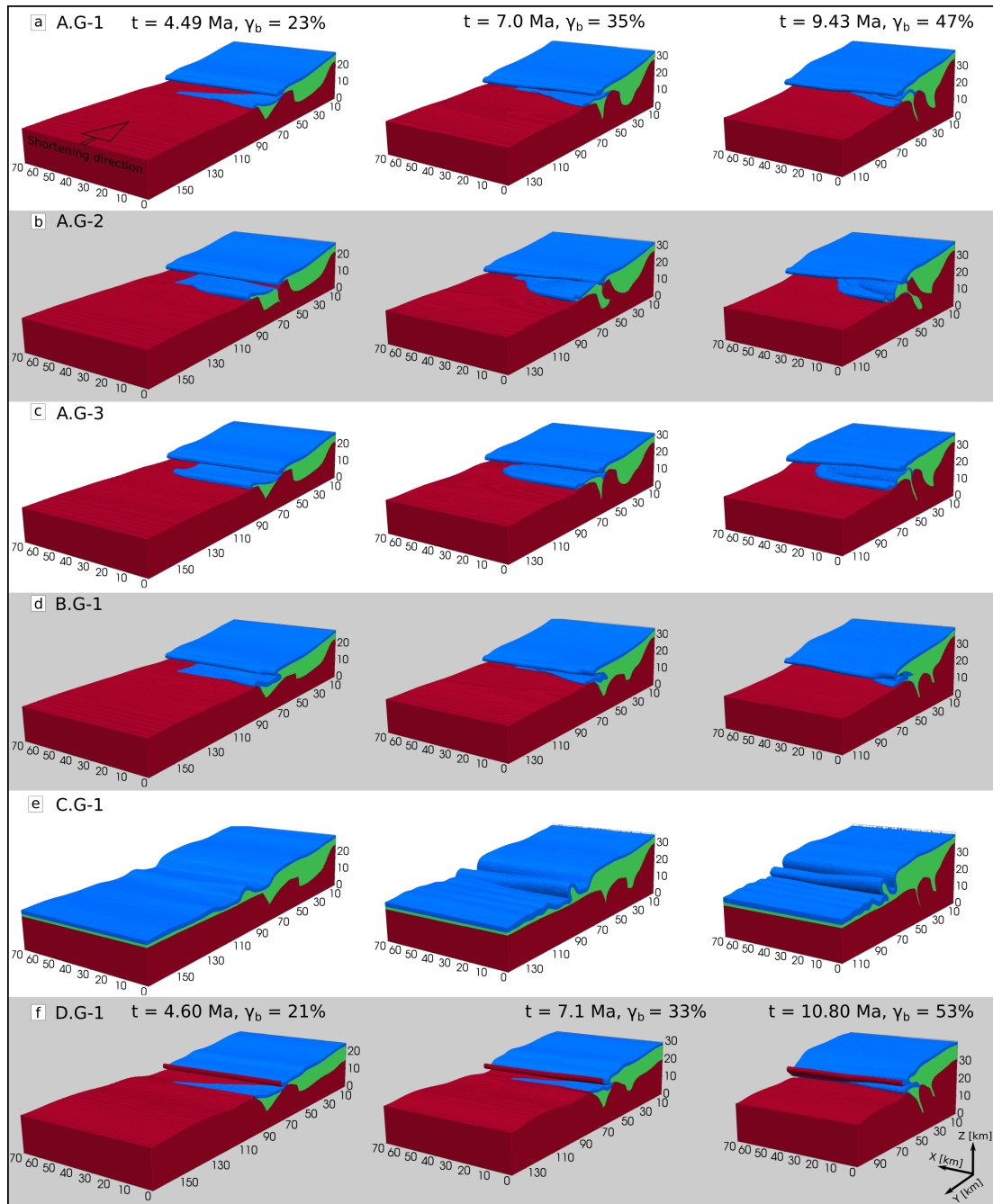
Figure 4. 3D model evolution for our six simulations, using a graphical threshold to highlight the deformation of the strong layer, weak units and the basement. Rows correspond to the configuration and columns to the total bulk shortening γ_b.

Model A.G-2 (Figure 4b) deviates in the structural evolution from model A.G-1. At 23 % bulk shortening (Figure 4b), the strong layer of HG is displaced more out of HG than for model A.G-1. The basement horst is slightly sheared towards the left, that is against the shortening direction. This shearing of the horst increases with progressive bulk shortening. At 47 % bulk shortening (Figure 4b) the HG is nearly closed at its top, but the closure of the HG did not form a cusp, as for model A.G-1.

305 In contrast, the sediments still in the HG become thicker with depth, because for the considered geometry of the HG it is more difficult to squeeze out all the sediments (Figure 4b). The strong layer of HG has been completely detached from the horst showing a higher slope in front of the extruded sediments. Overall, this model shows a significantly higher degree of basement involvement, with the up doming horst separating the nappe from HG from the thrust nappe from HB. Nevertheless, the front of the nappe from HB was displaced in the same uniform manner as in the reference model, A.G-1.

310 Model A.G-3 displays a similar evolution as model A.G-1 (Figure 4c). The geometry of HG results in a almost straight front of the squeezed out strong layer. There is a slight curvature at the lateral boundary between the lateral end of HG and basement (Figure 4c). The final stage (Figure 4c) shows a nappe originating from HG that is almost homogeneous in lateral X-direction. However, even though the depth of the half-graben is constant up to X = 50 km there is a notable decrease of nappe height from X = 30 to 50 km. This tilting of the nappe front towards the positive X-direction can be explained by the adjacent basement,

315 which might affect the degree of half-graben closure due to the strength contrast between the sediment and basement units. At 47 % bulk shortening (Figure 4c) the nappe from HB did not fully thrust over the fold nappe.

Model B.G-1 (Figure 4d) exhibits a continuous strong layer from HG to HB across the horst, but has the same geometry of HG than reference model A.G-1. At 23 % bulk shortening (Figure 4d) we observe a similar deformation of the strong layer at HG than in model A.G-1. However, a larger amount of weak sediments from HB is displaced across the horst against the

320 shortening direction. At 35 % bulk shortening the HG is less closed that for the same bulk shortening of the reference model (Figure 4d). Inside the initially continuous strong layer, a shear zone develops that forms a nappe of sediments from the region of the HB. At 47 % bulk shortening (Figure 4d) two nappe structures have formed; one consisting of sediments from HG and a structurally higher one consisting of sediments from HB. The two nappes are also stacked. However, in this model the strong layer has no connection anymore to the horst.

325 Model C.G-1 (Figure 4e), with a strong layer resting above the entire basement, shows detachment folding. The lateral variations in basement geometry are not significant enough to generate a shear zone in the strong layer, which eventually would form a nappe structure. The deformation of the basement and HG is similar to model B.G-1. The detachment fold with the largest amplitude originates from the region of HG (Figure 4e). With progressive shortening, this detachment fold is displaced across the basement against the direction of shortening (Figure 4e).

330 In model D.G-1 (Figure 4f), with a stress cut-off in the basement at 40 MPa, the shortening is more homogeneously distributed in the basement, so that during the initial stages of shortening (23 %; Figure 4f) the basement at large distance from the backstop is already thickened. Consequently, the basement uplift around the backstop is significantly lower compared to all other models. Furthermore, during nappe formation some parts of the uppermost basement are also sheared-off from the basement. The nappe forming from the strong layer of HG resembles a fold nappe.
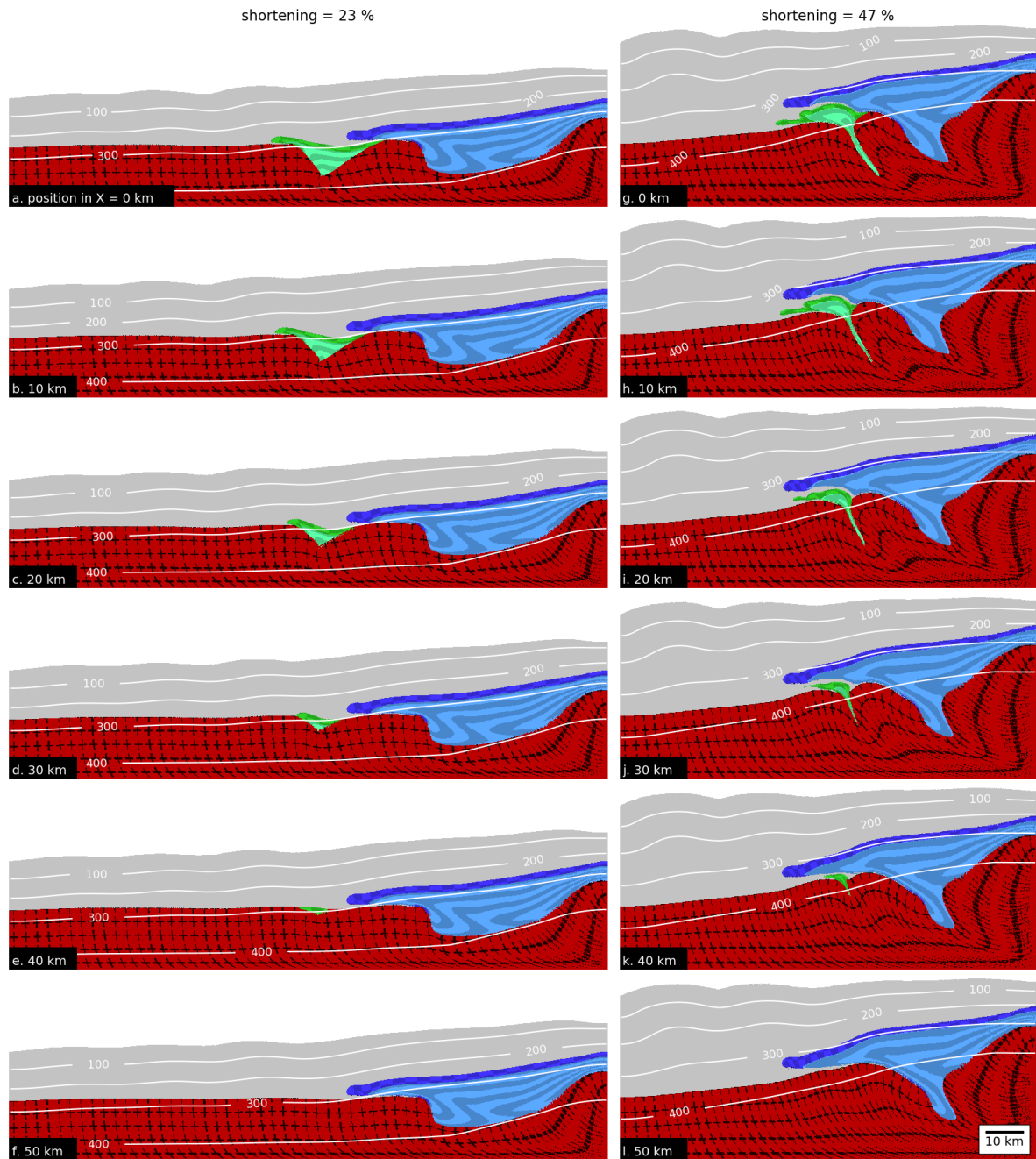
4.2 2D numerical cross sections

We discuss the deformation in the 3D models by analyzing six 2D cross sections parallel to the shortening direction (Y-direction) but at six different location along the lateral X-direction (Figure 5). The six cross sections are located along the lateral direction from X = 0 km to X = 50 km with 10 km spacing.

For the reference model A.G-1 (Figure 5) at 23% shortening (Figure 5, left column), the sediments from HB have been detached from their original position and thrusted across the basement horst all along the lateral direction (everywhere in the left column of Figure 5). The displaced sediments from HB resemble a thrust nappe. Around the backstop (right side) there is significant basement uplift. The cross sections show, from top to bottom, the shallowing and disappearance of HG. The strong layer is already sheared-out of HG, whereby the horizontal displacement is larger for deeper HG. Both nappes originating from HB and HG are deforming at the same time. The temperature around the top of the horst is ca. $300°C$.

The passive marker lines in the weak sediments of HB indicate ductile flow generating passive shear folds. In the basement the passive marker symbols ('crosses') indicate an increase in shear strain from the top to the bottom of the basement due to decrease in basement viscosity associated with a temperature increase. At 47% bulk shortening (Figure 5g-l, right column) the nappe from HB is thrust completely above the nappe from HG. The HG has been almost closed with the weak sediments residing now inside a cusp between the neighboring basement units, which dips towards the backstop. In the deeper region of HG the passive markers in the weak sediments indicate a fold nappe structure. The very frontal part of the nappe from HG resembles a thrust nappe, formed exclusively by the strong layer, whereas the main part of the nappe, including also the weak sediments, resembles a fold nappe (Figure 5g-i). Between the upper nappe from HB and the lower nappe from HG are cover sediments that have been dragged between the two nappes during overthrusting of the nappe from HB (Figure 5g-k). The nappe from HG disappears in lateral direction with the disappearance of HG. For the cross section without HG (Figure 5l) there is only a nappe from HB resembling a thrust nappe. Despite the significant lateral variation of the depth of HG and the associated lower nappe, the horizontal displacement of the upper thrust nappe is essentially the same along the lateral direction. Consequently, nappe formation of sediments from HG does not affect the horizontal displacement of the overthrusting nappe from HB. The horst exhibits a significant internal deformation in the regions with a deep HG, indicated by the passive marker symbols. The temperature isotherms are affected by the deformation and thickening of the model. Generally, the sediments are getting hotter during the deformation. At 23% bulk shortening the strong layer of HG has a temperature of ca. $300°C$ while the temperature of the strong layer of HB is less than $300°C$. At 47% bulk shortening the isotherms indicate that both strong layers were heated by ca. $50°C$.
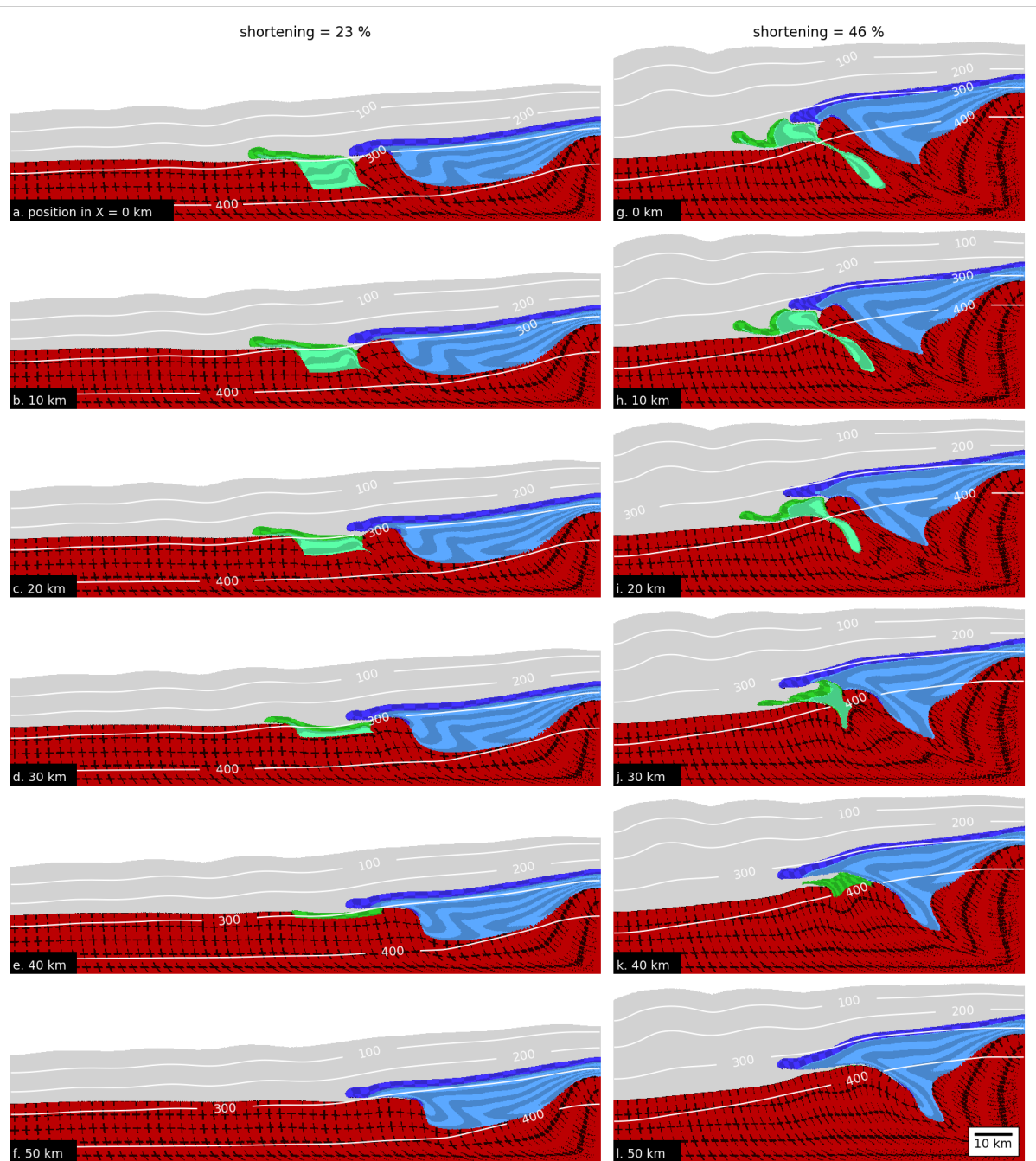
Additionally to the cross sections showing the structural and thermal evolution of model A.G-1, we display the same cross sections but indicating the magnitude of the deviatoric stress invariant, τ_{II}, to quantify the state of stress (Figure 6). The largest stress is ca. 140 MPa and occurs at the brittle-ductile transition in the cover, in a depth of ca. 5 km. At 23% bulk shortening (Figure 6a-f) the top of the basement exhibits τ_{II} values between 40 MPa and 80 MPa. After 47% bulk shortening τ_{II} values in the basement are strongly decreased, down to 10 MPa to 20 MPa, due to the increase of basement temperature. Overall, there are no considerable lateral variations in τ_{II}.

16

Figure 5. Graph showing lateral cross-sections for two different states of bulk shortening for the geometrical evolution of model A.G-1. Cross-sections are taken in 10 km steps from X = 0 km to X = 50 km. Additionally we display the isothermal lines in degree Celsius [$^{\circ}C$]. Columns correspond to the bulk shortening state and rows to cross-section X-position.
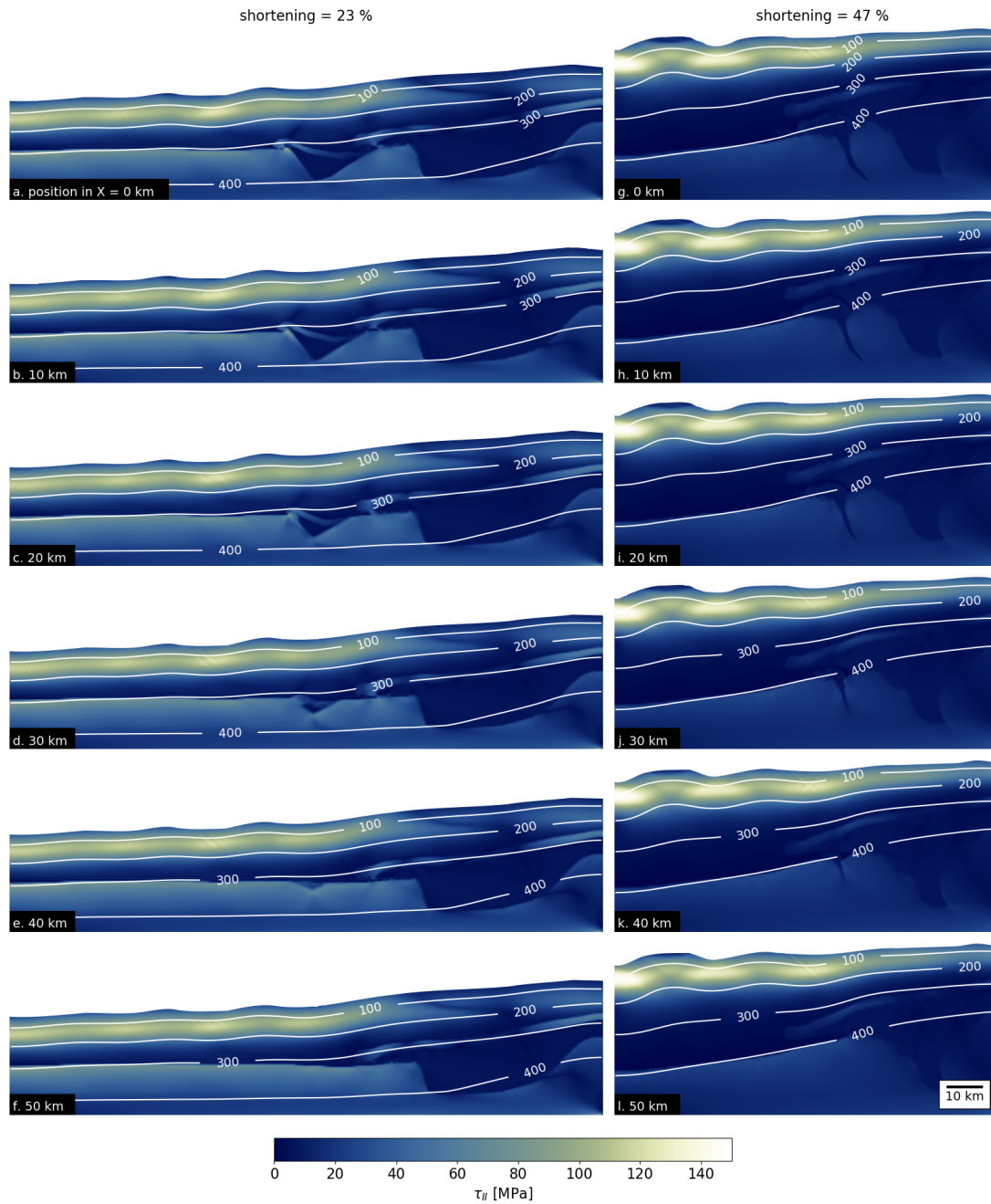
Figure 6. Graph showing lateral cross-sections for two different states of bulk shortening for the second invariant of the deviatoric stress τ_{II} of model A.G-1. Cross-sections are taken in 10 km steps from X = 0 km to X = 50 km. Additionally we display the isothermal lines in degree Celsius. Columns correspond to the bulk shortening state and rows to cross-section X-position.

Figure 7. Graph showing lateral cross-sections for two different states of bulk shortening for the geometrical evolution of model A.G-2. Cross-sections are taken in 10 km steps from X = 0 km to X = 50 km. Additionally we display the isothermal lines in degree Celsius $[°C]$. Columns correspond to the bulk shortening state and rows to cross-section X-position.

The cross-sections for model A.G-2 indicate overall a similar structural evolution as our reference model (Figure 7) in the sense that the sediments are sheared-out of HG and HB, form nappe-like structures and are piled at 46% bulk shortening. However, the different initial geometry of HG also generates differences in the structural evolution: At 23% bulk shortening the nappe from HB is less displaced across the horst for a deeper HG. The reason is that due to the different geometry of HG, the basement horst is also significantly sheared towards the left model side and represents, hence, a less stiff obstacle for a deep HG. Therefore, both the nappe from HB and the horst are sheared together towards the left model side. For a shallower HG, the horst represents a mechanically stiffer obstacle for the nappe from HB and, hence, the nappe is overthrust more to the left. At 46% bulk shortening (Figure 7g-l) we also observe extrusion of sediments from HG, but for the deepest regions of HG a significant amount of the sediments remains trapped between the basement at depth. Around the region where HG is deepest, the horst is sheared significantly and even sheared slightly on top of the basement that was initially to the left of HG (Figure 7g-i). The strong layer from HG is essentially disconnected from the horst and a significant part of this strong layer resembles more a thrust nappe. The temperature evolution of model A.G-2 is similar to the one of the reference model. The results indicate that the geometry of HG has a strong impact of the structural evolution of the nappes and the basement, although the first order structural evolution is similar to the reference model.

Model A.G-3 (Figure 8) shows a similar structural evolution as the reference model. The main difference can be observed in the cross section located at the lateral boundary of HG at X-position 50 km (Figure 8l). There, sediments of HG have been extruded laterally out of HG, which can be seen by a pocket of sediments inside the basement.

Model B.G-1 (Figure 9) shows a different nappe evolution than model A.G-1. At 23% bulk shortening (Figure 9a-f) in the region where the horst is overlain by weak sediments and a strong layer (*yellow*), the strong layer is sheared off the horst and pushed across HG by the strong layer from HB (Figure 9a). In the region where the horst is overlain only by the strong layer (*yellow*), the strong layer is continuously sheared and dragged by the sediments from HB (Figure 9b). The degree of shearing decreases with decreasing thickness of the yellow layer (Figure 9b-d). At 47% bulk shortening, HG is also almost closed and nearly all sediments have been squeezed out (Figure 9g-f). At X = 0 km (Figure 9f) the strong layer is completely detached from the basement. The layer initially resting on the horst has been sheared above the sediments from HG and is itself overthrust by the sediments from HB. This structure resembles the vertical stacking of three nappes whose sediments were originally horizontally next to each other. With decreasing thickness of the strong layer from the horst, its shearing across the sediments from HG is also decreasing (Figure 9i-k). Despite a horizontally continuous strong layer from HG to HB, a major shear zone developed in the strong layer and caused the generation of a nappe-like structure. The shear zone development inside the strong layer is only due to the geometrical variation of the underlying basement, because the strong layer has homogeneous material properties.

Model C.G-1, with a continuous strong layer across the entire model domain (Figure 10), shows a very different evolution compared to the reference model, because no prominent shear zones form in the strong layer, which could develop a nappe-like structure and significant overthrusting.

The strong layer initially above HG develops a detachment fold. At 23% bulk shortening (Figure 10a-f) this detachment fold already shows a great variability in amplitude in lateral X-direction of the model. During the initial stages of folding, the
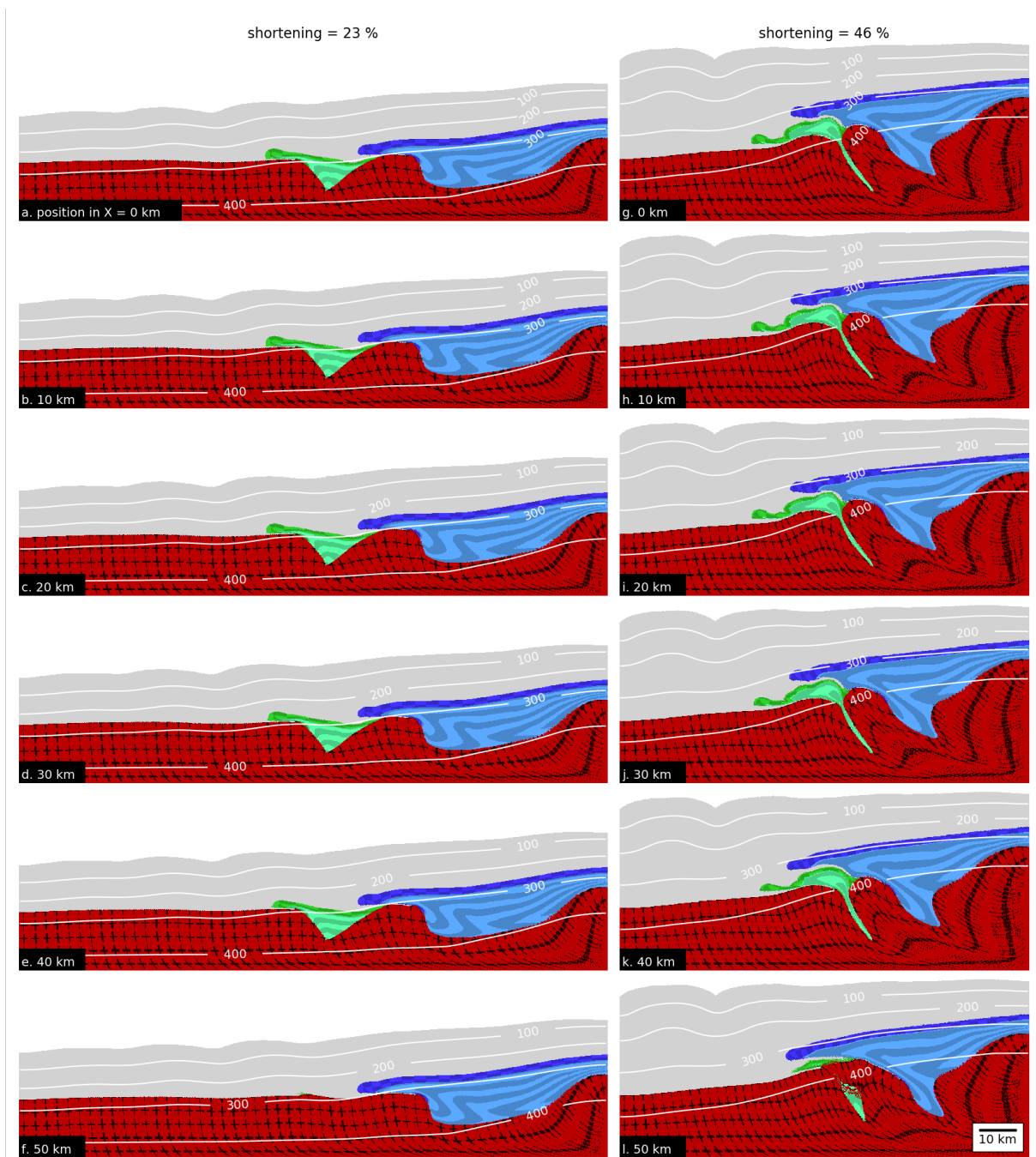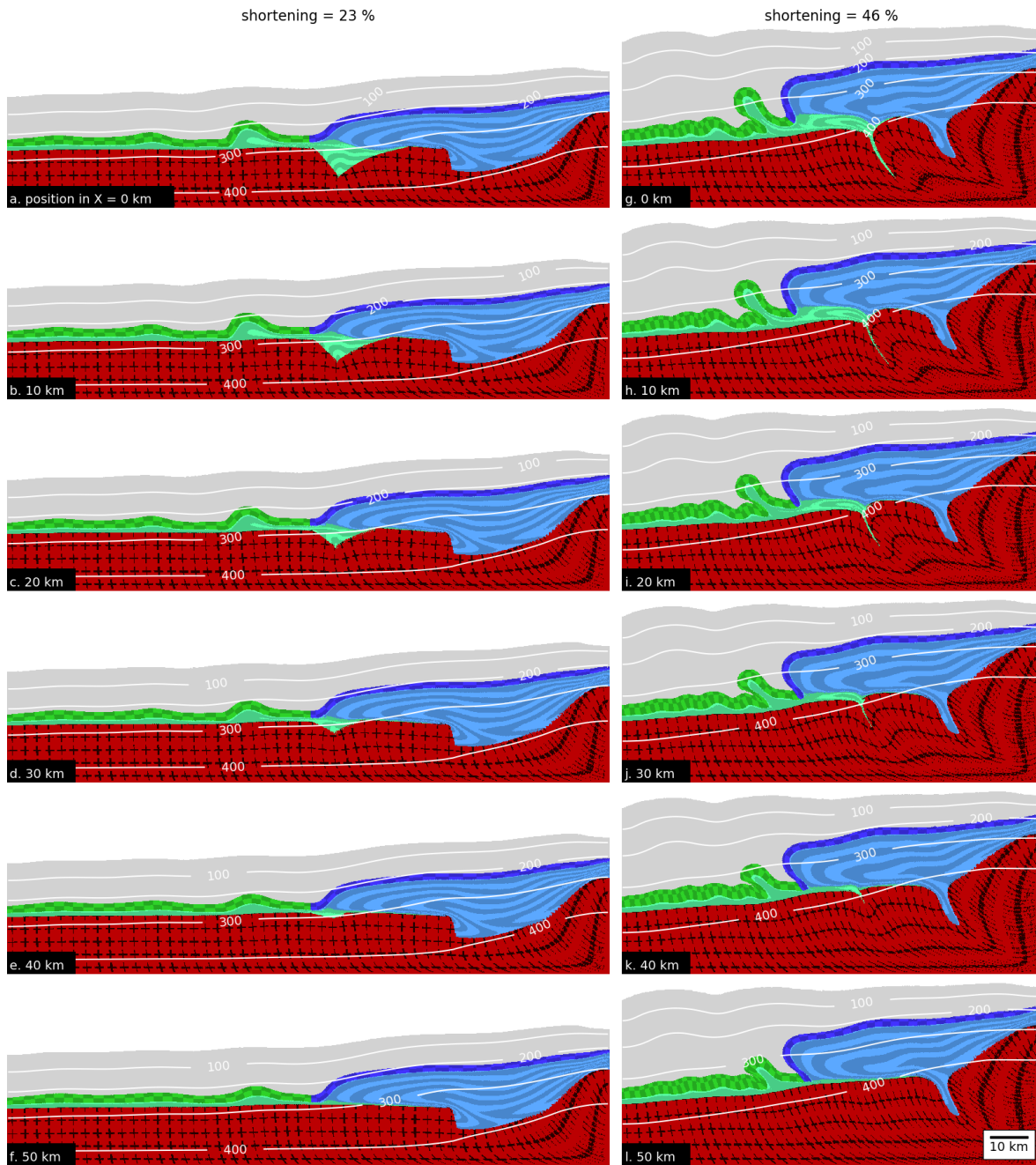
Figure 8. Graph showing lateral cross-sections for two different states of bulk shortening for the geometrical evolution of model A.G-3. Cross-sections are taken in 10 km steps from X = 0 km to X = 50 km. Additionally we display the isothermal lines in degree Celsius [$^{\circ}C$]. Columns correspond to the bulk shortening state and rows to cross-section X-position.
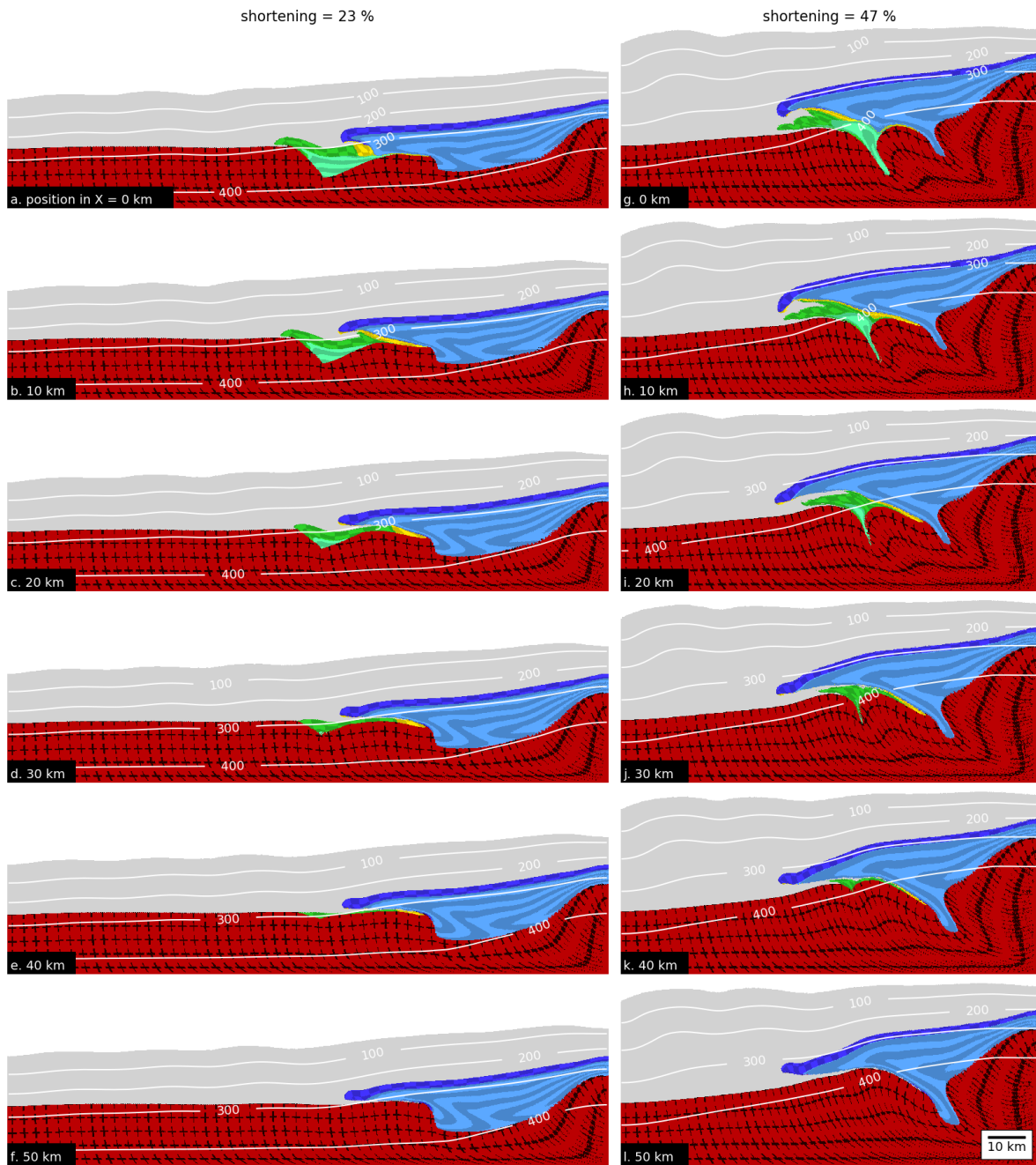
Figure 9. Graph showing lateral cross-sections for two different states of bulk shortening for the geometrical evolution of model B.G-1. Cross-sections are taken in 10 km steps from X = 0 km to X = 50 km. Additionally we display the isothermal lines in degree Celsius $[^{\circ}C]$. Columns correspond to the bulk shortening state and rows to cross-section X-position.

Figure 10. Graph showing lateral cross-sections for two different states of bulk shortening for the geometrical evolution of model C.G-1. Cross-sections are taken in 10 km steps from X = 0 km to X = 50 km. Additionally we display the isothermal lines in degree Celsius [°C]. Columns correspond to the bulk shortening state and rows to cross-section X-position.

core of this fold was filled with half-graben sediments and progressively displaced towards the left where the basement top is horizontal (Figure 10a-e). In the region without half-graben, only a small amount of weak sediments was available to fill the fold core so that considerable amplification was inhibited (e.g. cp. Figure 10f and a), as is the case for detachment, or décollement, folding (e.g. Epard and Groshong Jr, 1993; Schmalholz et al., 2002; Butler et al., 2019). During bulk shortening, the detachment fold is displaced across the basement towards the left. The HG is also closed after 47% bulk shortening (Figure 10g-j). Similarly to the other models the weak half-graben sediments have been extruded and some of these sediments have filled the core of the detachment fold. The green marker lines in Figure 10g indicate that the fold was continuously fed by the half-graben sediments during ongoing deformation. Hence, the amplitude of the largest individual fold decreases towards the model side without a half-graben (Figure 10g,l). The strong layer initially from HB forms a thick nappe-like structure with a slightly overturned layer at the front. However, no overthrusting above the sediments from HG occured.

Compared to the reference model, model D.G-1 (Figure 11) shows only a minor basement uplift at the right boundary at 21% bulk shortening (Figure 11a-f). Instead, the bulk shortening is distributed more homogeneously throughout the basement, resulting in significant thickening also in the basement on the left model side. Because the top of the basement is weaker, the strong layers can shear-off and displace slices of the basement (e.g. Figure 11a). Further bulk shortening results in the extrusion from sediments from HG resulting in a structure resembling a fold nappe. This fold nappe is overthrust from the sediments from HB, resembling a thrust nappe (Figure 11g-l). The last deformation stage is shown for 53% bulk shortening, because $6-7\%$ more bulk shortening is required to overthrust the sediments from HB, compared to the reference model. The strong layer from HG forming the fold nappe exhibits an overturned limb that is still in contact with the basement. Thus, this model does not form any structure similar to a thrust nappe for the sediments from HG. The passive marker symbols show gentle folding of the basement, also on the model side without half-graben (Figure 11l). In contrast, the reference model (Figure 5l) exhibits updoming of the basement without well developed folding.

4.3 Nádai strain and Lode's ratio

We compute the Nádai strain ε_s (Nádai and Hodge, 1963) and Lode's ratio v (Lode, 1926) for our simulations, which are two quantities to quantify 3D finite strain. Both parameters are computed from the natural logarithm of the finite strain principal axes, $\varepsilon_1, \varepsilon_2$ and ε_3. The Nádai strain ε_s is the octahedral shear strain and provides a non dimensional value for the strain magnitude:

$$\varepsilon_s = \frac{1}{\sqrt{3}} \sqrt{(\varepsilon_1 - \varepsilon_2)^2 + (\varepsilon_2 - \varepsilon_3)^2 + (\varepsilon_3 - \varepsilon_1)^2} \tag{7}$$

The Lode's ratio provides information on the strain symmetry and strain regime and can exhibit values in the interval of $[-1\ 1]$. In particular, $v < 0$ indicate a prolate strain ellipsoid (constrictional strain), $v = 0$ a prolate-oblate strain ellipsoid (plane strain) and $v > 0$ an oblate strain ellipsoid ellipsoid (flattening strain):

$$v = \frac{2\varepsilon_2 - \varepsilon_1 - \varepsilon_3}{\varepsilon_1 - \varepsilon_3} \tag{8}$$
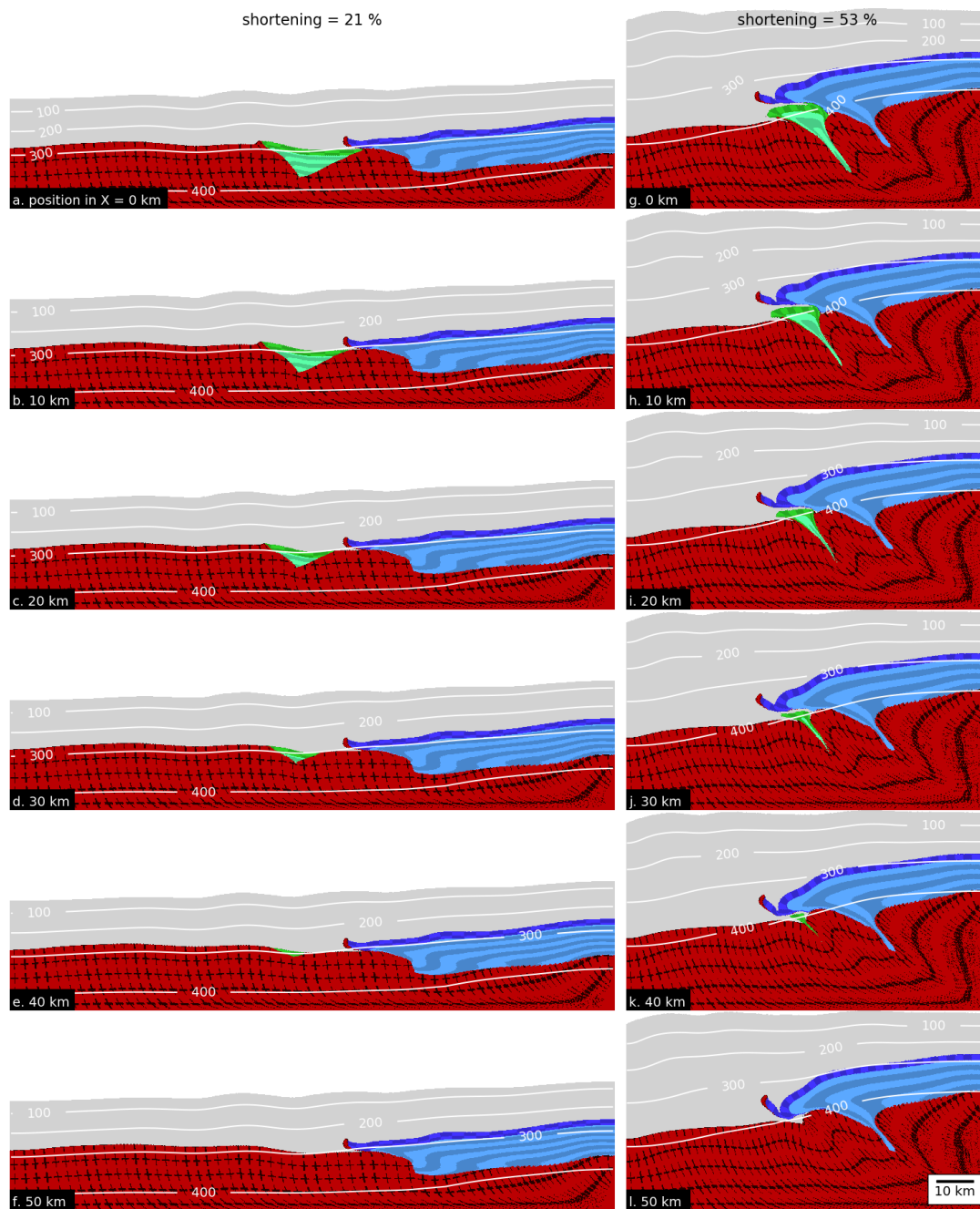
Figure 11. Graph showing lateral cross-sections for two different states of bulk shortening for the geometrical evolution of model D.G-1. Cross-sections are taken in 10 km steps from X = 0 km to X = 50 km. Additionally we display the isothermal lines in degree Celsius $[^\circ C]$. Columns correspond to the bulk shortening state and rows to cross-section X-position.

We display both quantities for model A.G-1 (Figure 12) for three different cross-sections, which provides a representative image of the finite strain distribution also for the other models. The first section is taken at the maximum depth of HG (X = 0 km), the second at half of the depth (X = 25 km), and the last at the section where the half-graben disappears (X = 50 km). In general, ε_s values are highest on the right side on top of the basement horst, ranging between 3.5 to 4. The extent of this shear zone, for the same intensity, changes laterally with changing depth of HG. For example, the shear zone roots much deeper into the basin on the side without HG (cp. Figure 12a-c). Moreover, ε_s outlines the fold nappe structure indicating that the fold nappe is surrounded by highly strained material. Here, maximal values of ε_s increase laterally with decreasing depth of HG. Another lateral difference is the intensity of the shear zone located on the left side of the model in front of the extruded sediments. This shear zone also gains intensity in lateral direction with decreasing half-graben depth. Similarly to ε_s the, Lode's ratios ν (Figure 12d-f) pinpoint the shear zone on top of the horst and outline the fold nappe.

Overall, ν values are close to zero which indicates a plane strain deformation. The largest deviations from plane strain are located in the cross section of maximum depth of HG (Figure 12d). Furthermore, values around the fold nappe in the range of 0.5 imply a flattening regime. In contrast, the shear zone at the rear of the basement horst displays negative values that are in the order of -0.2 to -0.5, indicating a constrictional deformation.

5 Discussion

5.1 Impact of lateral geometry variations and rheological layering

Our models show the detachment of sedimentary units and their subsequent horizontal transport. Depending on the model configuration, the sedimentary units resemble fold or thrust nappes. The strain localization necessary to detach the sedimentary units and to transport them horizontally without significant internal deformation occurred without any mechanical softening. In our models, the main cause of the strain localization is the initial geometrical configuration and the variations of mechanical strength between the model units. Strain localization and associated shear zone formation due to geometrical and strength variations has been shown with 2D numerical simulations to occur even for linear viscous material (Bauville and Schmalholz, 2017). For such strain localization no variation of effective material properties develops and it is, hence, sometimes termed kinematic strain localization, which is fundamentally different to so-called dynamic softening mechanisms in which the effective material properties change, for example due to local heating, grain size reduction or fluid infiltration (Bauville and Schmalholz, 2017). Moreover, the formation of fold nappes by pushing ductile material against a rigid obstacle, without dynamic softening, was shown, for example, with laboratory deformation experiments (e.g. Bucher, 1956) and numerical simulations (e.g. Peña and Catalán, 2004). Dynamic softening mechanism are most likely active in nature, but their intensity and the required deformation conditions are still contentious. Furthermore, dynamic softening mechanisms most likely intensify the strain localization shown in our models, but our models show that, in principle, such dynamic softening mechanism are not essential to generate nappe-like structures.

26
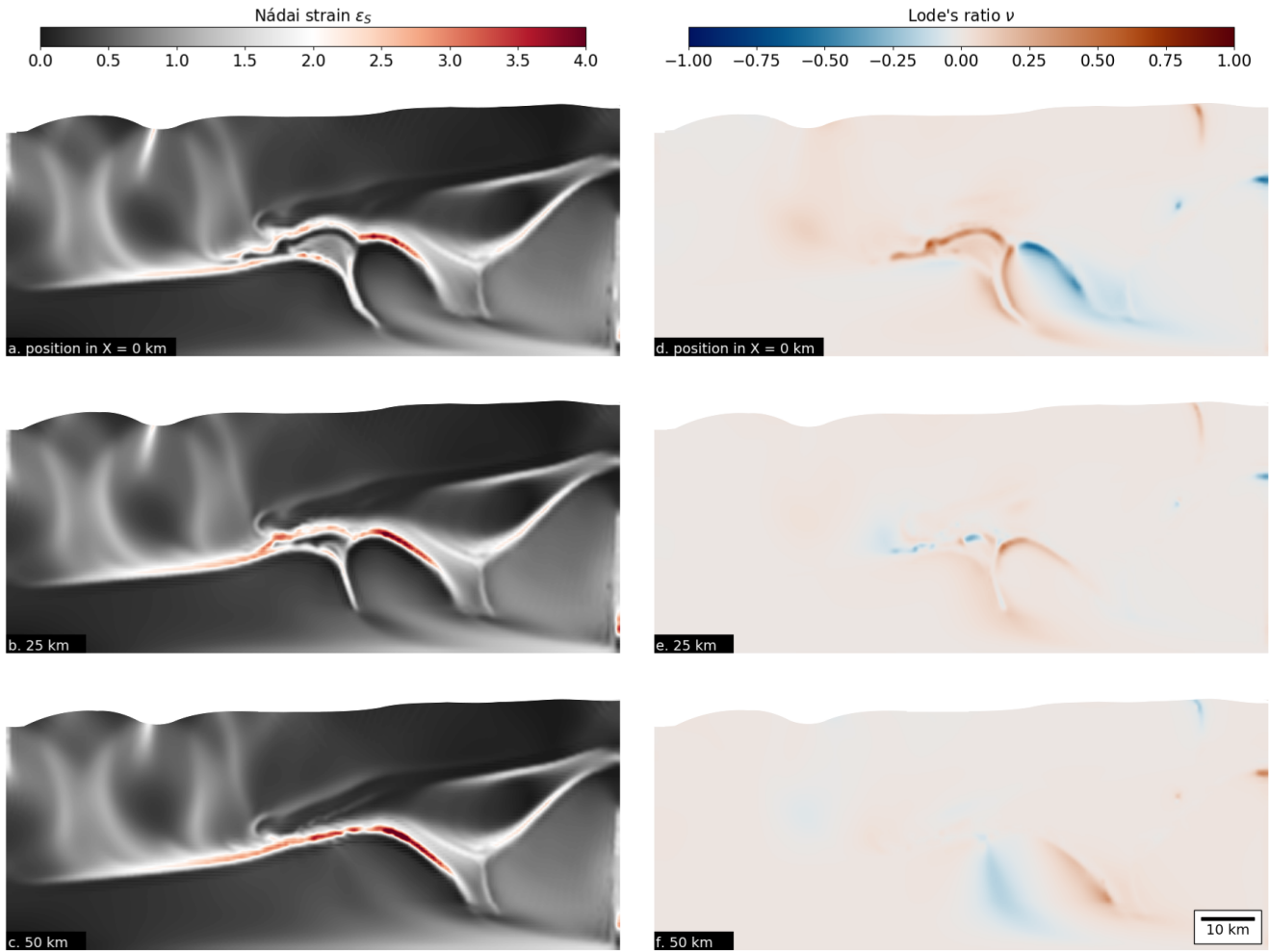
Figure 12. Graph showing three different cross-sections of model A.G-1 displaying Nádai strain (first column) and Lode's ratio (second column). Row-wise cross-sections at X = 0, 25, 50 km, respectively.

The emplacement of the sediments from HB in the style of a thrust nappe is observed in all models with exception of model C.G.-1. The thrust nappe exhibits a laterally uniform front despite the deformation and nappe formation in HG below (Figure 4). Even in the case of model A.G-2, where the basement horst is strongly incorporated in the deformation, we do not observe large horizontal displacement gradients in the thrust nappe. Hence, deformation of such relatively small graben systems might play only a minor role on the displacement variations along strike of fold-and-thrust belts. In our models, the uniform thrust front is the result of the initially straight boundary between basement horst and HB. Consequently, we infer that the initial large scale basin architecture plays a major role in the geometry of orogenic salients. Several studies (e.g. Thomas, 1977; Marshak et al., 1992; Boyer and Elliott, 1982) of different orogens also indicate that the sediment basin thickness is of particular importance in the expression of salients. In the context of thickness variation, Macedo and Marshak (1999) investigated the effect of

27

variable basin geometries during bulk shortening using 3D sandbox models. Their study implies that basin-controlled salients are strongly controlled by the basin topography, that is, variations of sedimentary thickness inside the basin. This observation is in accordance with our study which shows that lateral changes in the lithology, such as thickness and rheology, produce different salients (5). There are, however, additional conditions such as the indenter shape or the direction and orientation of convergence of the colliding plates that influence the overall shape of orogens (e.g. Laubscher, 1972; Ries, 1976; Mitra, 1997). Naturally, the investigation of such large scale boundary effects would require a different model configuration than in our study. Volume variations related to the lateral changes in the depth of HG are always expressed in the lateral variations of the thickness of the extruded nappe. The thinning out of the initial graben structure is reflected in a decrease of height and a decrease of length of the nappe. These lateral variations also affect the lateral amplitude variation of the major detachment fold of simulation C.G-1. The local geometry around the major detachment fold resembles a thin skinned tectonic style where most deformation is concentrated in the cover sediment. However, much of the sediments filling the core of the detachment fold originate from HG, which is more than 10 km away from the detachment fold (Figure 11g-l). Closure of HG resulted in movement of sediments from HG into the core of the detachment fold. This result shows that detachment fold initiation and progressive evolution can be controlled by the inherited basement structure, Additionally, this finding suggest that predominately thin skinned tectonics can passively be influenced by underlying heterogeneities due to variations in the basement architecture. Nevertheless, the expression of such detachment folds in our models also depends largely on the thickness ratio between incompetent and competent units. Our findings are, therefore, in broad agreement with previous field observations and numerical studies (e.g. Pfiffner, 1993; Jaquet et al., 2014).

5.2   Comparison with the Helvetic nappe system

Model A.G-1 and B.G-1 are able to reproduce several first-order structural features of the Helvetic nappe system. In addition, we are also able to connect the two different main kinematic deformation phases of the Western Helvetics and the Eastern Helvetic Nappes. The formation of the main basal thrust originates in weak sedimentary units, comparable to the Cretaceous Palfris shales, of our Helvetic basin equivalent. Similarly to the Prabé deformation phase in the West and the contemporaneous Calanda phase in the East (e.g. Pfiffner, 2015), this basal thrust aids in the transport of a laterally uniform thrust nappe in our simulations. Given the simplifications of our model, we attribute the resulting major thrust front to the formation of basal thrust of the Wildhorn super-nappe in the West and the Glarus thrust in the East. Continuous bulk shortening leads to shear localization at the contact between the strong layer and the horst in the basin. Subsequently, the layer is detached and translated with the help of the weak sediments across the basement horst and onto the half-graben, resembling a thrust sheet or nappe. We record a first noticeable deformation of the half-graben approximately 2 Ma in our simulations. This timing is in agreement with a study by Jaquet et al. (2018) which proposes a similar time interval between the onset of the Helvetic nappes and the onset of the basal thrusting at the Morcles half-graben. Continuing, the vertical extrusion and squeezing-out of the half-graben sediments takes place simultaneous with stacking of the major thrust nappe on top at about 6 to 7 Ma. The resulting model nappe stack shows laterally major structural differences. The overall along-strike variation is comparable to the lateral structural
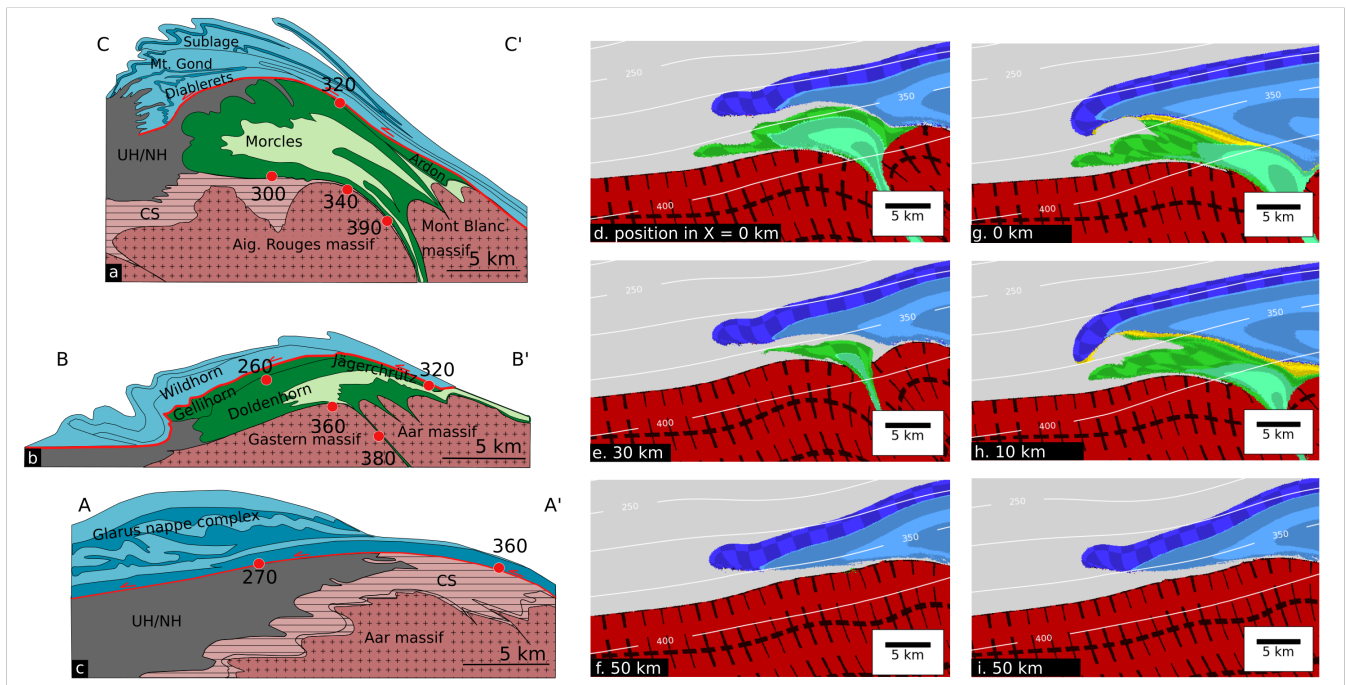
Figure 13. Comparison between the geological cross-sections of the Morcles nappe, Doldenhorn nappe and Glarus nappe complex with sections taken from our numerical simulations. Columnwise(left to right) 1.column: geological-cross sections, 2.column: sections from model A.G-1, and 3.column: sections from model D.G-1. Temperatures taken from Ebert et al. (2008). UH/NH = Ultrahelvetics/North Helvetics. CS = Cover sediments.

variations in the Helvetic nappe system, where the prominent fold nappes are only located in the southwest (Pfiffner, 1993). At the end of our simulations we record approximately 10 Ma for the complete process of nappe stack formation. This timing is

510 in broad agreement with studies of the Morcles nappe complex (e.g. Kirschner et al., 1996; Boutoux et al., 2016) that suggest an emplacement duration of 10 to 15 Ma.

Figure 13 shows a comparison between geological cross-sections taken along-strike of the Helvetic nappe systems with selected enlarged numerical cross-sections in lateral direction of our model. The first cross-section a) of model A.G-1 (Figure 13d,e,f) shows our equivalent of the Morcles nappe at the maximum depth of the half-graben. The result here is similar to 2D numerical

515 studies by Bauville and Schmalholz (2015) who investigated fold nappe formation and nappe stack formation also in application to the Helvetic nappe system, respectively. To first order we reproduce an extruded fold nappe with a shape comparable to first order to the Morlces nappe.

The strong layer is still connected to the adjacent basement horst and the deformed internal weak units, highlighted by the green passive marker lines, resemble a recumbent fold. The inner part of the fold nappe roots into a steep cusp which is

520 analogues to the Chamonix zone between the Aiguilles-Rouges and Mont Blanc massif (Figure 13a). The Chamonix zone is often interpreted as a syncline (Paréjas, 1922; Oulianoff, 1924; Ayrton, 1980; Ayrton and Jemelin, 1987), however, other
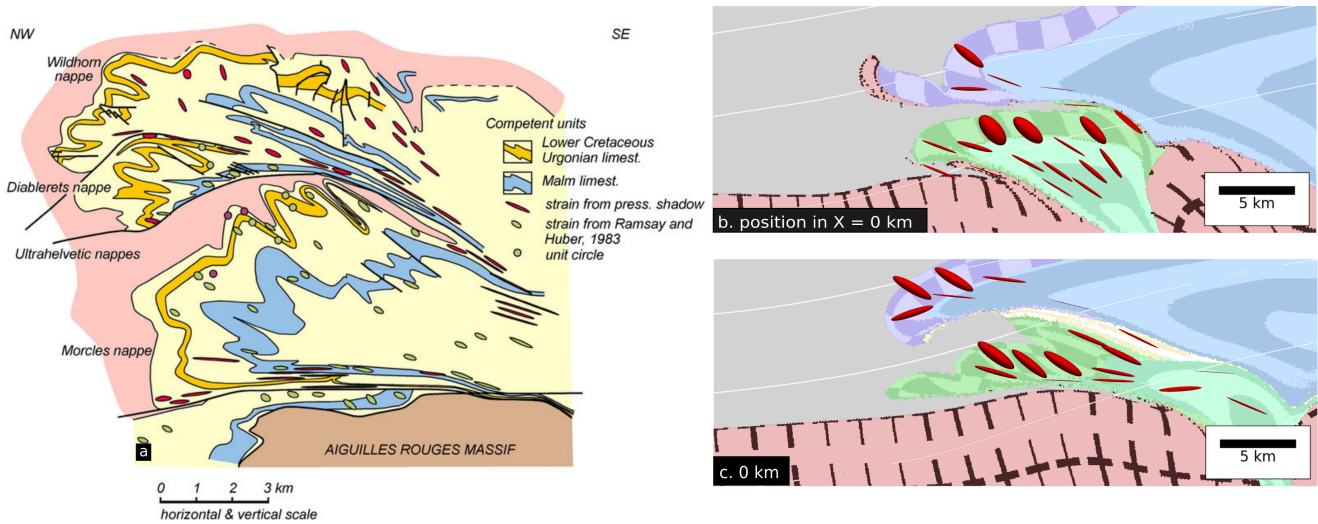
Figure 14. Comparison between finite strain from the Morcles nappe (taken from Bastida et al. (2014) showing a recolored version of the synthetic cross-section with strain ellipses from pressure shadows after Casey and Dietrich (1997) including green strain ellipses from Ramsay and Huber (1987), the cross-section is modified from Dietrich and Casey (1989)) and selected finite strain ellipses from model A.G-1 and model D.G-1.

interpretations propose that there is a continuous younging direction in the sediments of the Chamonix zone, from the Mont Blanc massif towards the Aiguilles-Rouges massif (Pfiffner et al., 2011).

Moreover, we find significant amount of material from the overburden between the thrust nappe and the fold nappe, but also below the fold nappe. The material between the two nappes resembles the Ultrahelvetics in the geological cross-sections, whereas the material below the fold nappe corresponds to undeformed cover-sequences of the basement. Turning now to the Morcles equivalent of model B.G-1 (Figure 13g) we find a significantly different structure of the extruded fold nappe. There are several major differences that are connected to the initial mechanical layering inside the half-graben. First, the fold nappe shows a far greater length to height aspect ratio than the natural analogue. Secondly, the strong normal limb is not in contact with the basement horst. Due to the continuous strong layer the structure shows greater shearing at the contact between the fold and thrust nappe.

Proceeding with cross-section e) of our numerical model A.G-1 (Figure 13e), we find similarities with the geological cross-section of the Doldenhorn nappe (Figure 13b). The extruded nappe shows similar aspect ratio and shape like the Doldenhorn nappe with the length significantly exceeding the thickness. However, cross-section h) of model B.G-1 (Figure 13h) provides an even better match with the structure of the Doldenhorn nappe. The resulting fold nappe shows a comparable shape and size. Due to the initial rheological layering this model forms a thin thrust sheet on top of the fold nappe. We interpret this thrust sheet as an analogue to the Gellihorn and Jägerchrütz nappes, which are essentially thin thrust sheets on top of the Doldenhorn nappe (Pfiffner et al., 2011).

30
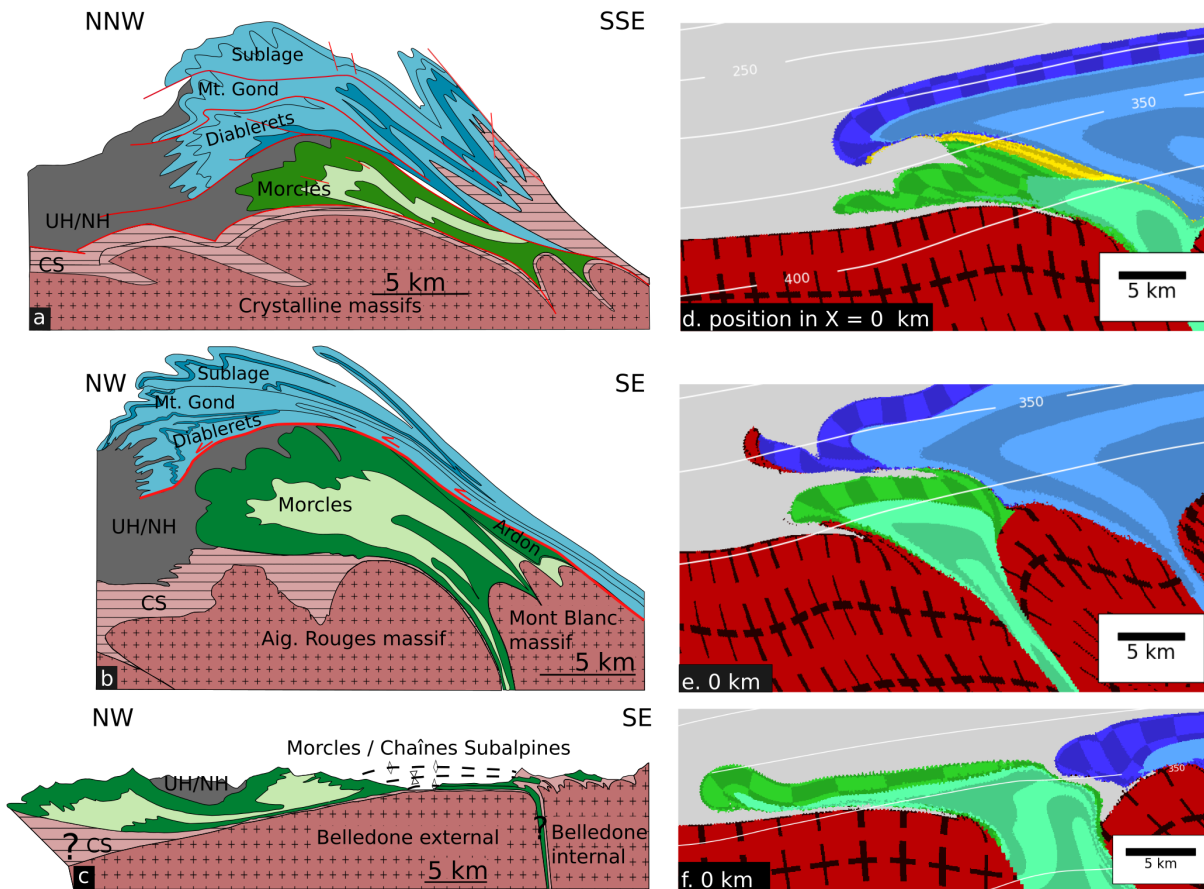
Figure 15. Comparison between selected numerical cross-sections and simplified geological cross-sections. Row-wise(top to bottom) a) Simplified Morcles section modified after Pfiffner (2015) (indicated in the map of Figure 1 with the dashed profile line) and d) section from model D.G-1. b) Simplified Morcles modified section after Escher et al. (1993) and e) cross-section model F.G-1. c) Simplified section modified after Epard (1990) and f) section from model A.G-2. UH/NH = Ultrahelvetics/North Helvetics. CS = Cover sediments.

Finally the numerical cross-sections without half-graben (Figure 13f,i) exhibit a similar displacement and shape for both of our

540 models. The finding suggests that underlying nappe formation in HG and minor variations in the vertical rheological layering has a negligible effect on the horizontal displacement parallel to the shortening direction along strike of the major thrust sheet. To first order, this structure is comparable to the Glarus nappe complex displayed in Figure 13c.

Additionally, we also find a first order agreement when comparing the finite strain pattern between field measurements from the Morcles nappe and our numerically calculated finite strain (Figure 14). Generally, the aspect ratio of the strain ellipses increases

545 towards the bottom and root zone of the nappe, indicating significant shearing. Furthermore, we observe less deformed ellipses in the top, normal limb of our Morcles equivalent with ellipses of higher aspect ratios (Figure 14b, d) near the contact between

31

the fold nappe and the thrust nappe. Figure 14b shows a better match for the finite strain pattern in the upper limb, whereas Figure 14c displays a better fit for the contact zone. We also observe a subhorizontal orientation of the major finite strain axis towards the root zone of the nappe (Figure 14c). Numerical finite strain computation is a useful tool to compare numerical models with natural observations. The comparison can efficiently be used to recognize where the numerical model requires adaptation to the real data.

However, certain first order features of the Helvetic nappe system we could not reproduce with our models. The first shortcoming is the protrusion and shearing out of the strong layer of the half-graben. In 3D view this process is expressed as a thin carpet in front of the fold nappe (e.g. Figure 4c,f), resembling a nose-like feature in the 2D cross-sections. Shearing out of the layer inhibits the formation of an outer recumbent limb as observed in the Morcles nappe (Ramsay et al., 1983). Here, our results are in contrast with previous 2D thermo-mechanical numerical modelling results by Bauville and Schmalholz (2015), who successfully simulated the formation of a recumbent fold limb during half-graben inversion. One of the main reasons for this deviation lies in the viscosity ratio (η_R) between overlying strong layer (η_L) and the half-graben infill (η_I). In the simulations of Bauville and Schmalholz (2015), both the layer and the infill have the same viscosity ($\eta_R = 1$), whereas our simulations, using different creep flow laws for each units, show that the infill viscosity η_I can be up to three orders of magnitude smaller than the strong layer viscosity η_L ($\eta_R = 1000$). Secondly, temperature estimates from several authors (e.g. Kirschner et al., 1999; Herwegh and Pfiffner, 2005; Ebert et al., 2007b) indicate lower peak temperature conditions along the different basal nappe contacts in comparison with our simulations. For example, Ebert et al. (2008) report increasing temperatures of $270°C$ to $390°C$ from the frontal part of the Morcles nappe to its root. Here we find a close match with root zone temperatures, whereas our front part of the fold nappe exhibits temperatures in the range of $370°C$ (e.g. Figure 13d). Similar temperature comparisons between our Doldenhorn and Glarus nappes equivalents show the same trend (see Figure 13). Moreover, the cross-sections of model B.G-1 exhibit slightly higher temperatures inside the core of the fold nappe, in consequence of the significantly thicker thrust nappe above. In summary our models show a good match for the root zone temperatures, but higher temperatures at the front of the nappe complexes compared to natural observations. Ebert et al., 2008 suggest a horizontal temperature gradient of approximately $6°C/km$ along the nappe interface for all three cross-sections. We only register a horizontal gradient of $2°C/km$ along the basal thrust surfaces. Additional constraints are given by Leloup et al. (2005) and Boutoux et al. (2016) who indicate peak metamorphic temperatures of $320°C$ for the Aiguilles-Rouges massif and $400°C$ for the Mont Blanc massif. Despite these discrepancies our model conforms to the temperature trends of natural observations, showing increasing temperatures from the front to the root zones of the nappes. Further improvements could be made by adjusting the initial geothermal gradient or by modifying the initial geometrical configuration. For the latter case, primarily, Nibourel et al. (2018) demonstrate that the Aar massif experienced a $10 - 15°$ southwards dip in relation to the isotherms. Essentially such a configuration would, for example, place the half-graben system further up in the isotherms. This adjustment would lead to cooler temperatures in the front of the nappe and greater horizontal temperature gradients during and after nappe emplacement.

In terms of large scale structural components our simulations lack the formation of parasitic folds, smaller imbricate thrusts or the detachment between different levels inside the major thrust complex. Modelling of such smaller-scale features would require (i) a higher numerical resolution in combination with (ii) a drastically more complex rheologically layering. In addition,

field observations indicate the existence of several large scale shear zones in the Mont Blanc and Aar massif. Our models do not reproduce such features, mainly because of our mechanically homogeneous basement unit which represents a large simplification compared to the natural complexities. There are, for example, several studies regarding the Aar massif that correlate the formation of ductile and brittle shear zones to inherited pre-alpine heterogeneities (e.g. Berger et al., 2017; Mair et al., 2018). In particular, structures such as foliations, mafic dykes or folds present mechanical anisotropies that can culminate in localized strain and shear zones (e.g. Bell, 1978; Carreras et al., 2010; Herwegh et al., 2017; Wehrens et al., 2017). Finally, our model does not fully resolve the large scale kinematics and intricate deformational history of the Helvetic nappe system. For example, reconstructions between the SW and the NE of the Helvetics show a differential horizontal displacement of the thrust nappes of up to 50 km (e.g. Pfiffner, 2015). Here, variations are likely due to the initial basement geometry and convergence of subducting plate e.g. obliquity of the plate which have not been taken into account in our model.

5.3   Comparing geological with modelled cross sections: The Morcles nappe

We show and compare three different, simplified geological cross sections of the Morcles nappe with our numerical results (Figure 15). The cross sections are from different locations along strike of the Morcles nappe and highlight, together with our numerical cross sections, the lateral variability of the Morcles nappe. Differences in the presented geological cross sections most likely do not exclusively indicate true lateral variations in the tectonic structures, but may also result from different geometrical projection methods and different geological interpretations. Such potential apparent differences should be kept in mind when comparing numerical models with constructed geological cross sections, which can be considered as geometrical models that are also based on assumptions like the numerical models. We start with a comparison of a geological cross section of the Morcles nappe near the Sanetschpass and a section of model B.G-1 (Figure 15a and d). Here, the geological cross section shows a relatively thin Morcles nappe with a sheared lower and upper limb. This observation is similar to our cross section which exhibits an elongated sheared fold nappe with sheared lower and upper limbs. Moreover, in this model we observe a significant deformation of the basement at the contact of the cover sediments which is in agreement with microstructural observations that suggest a brittle-ductile emplacement of the Morcles nappe (Ebert et al., 2007a; Austin et al., 2008). Figure 15b shows a Morcles cross section of Escher et al. (1993) from further Southwest in the nappe system. In this case, model D.G-1 (Figure 14e) provides a better first order fit than B.G-1. Our fold nappe exhibits a strongly sheared recumbent limb that still reaches into the root zone of the nappe. Furthermore, the strong layer is still connected to the basement horst and is in contact with the thrust nappe where it is sheared, displaying a similar saw-tooth shape as observed in the geological cross section. Also, the overall aspect ratio is closer to the geological cross-section than in model B.G-1. In contrast, both of the previous numerical sections do not match the observations for the nappe structure even further Southwest in France near Megève (Figure 15c). We assume that in this region the Morcles nappe and the Chaînes Subalpines constitute one large tectonic nappe that derived from the North Helvetic basin. Here, the sediments are rather squeezed out of the half-graben due to a greater thickness of shales instead of forming a recumbent limb (Epard, 1990). Therefore, we suggest that a cross-section of model A.G-2 Figure (15f) shows a closer match to the geological structure. In summary, different cross sections of the Morcles

33

615   nappe can be compared to different numerical models with different initial conditions regarding the geometry or rheology. Hence, it is a challenge to capture the evolution of 3D geological structures with a single 3D model, because of the geometrical and rheological uncertainties. Further, this also implies that one has to be even more cautious in the application of a single 2D model to the formation of 3D fold-and-thrust belts and geological structures in general.

6   Conclusions

620   The presented 3D numerical simulations show the formation of a fold-and-thrust belt resulting from the wedge-type deformation of the upper crustal region of a passive margin. The formation of the sedimentary nappes results from the shearing-off and detachment of sedimentary units form the half-graben, horst and basin. Nappe detachment, transport and stacking occur for standard viscoplastic rheological models without any applied rheological, or dynamic, softening mechanisms. Nappe formation and their geometry are controlled by the initial basement geometry and the strength contrast between basement and

625   cover sediments and the strength contrast within the sediments. The results indicate the fundamental importance of tectonically inherited structures on the evolution of fold-and-thrust belts. Consequently, the results emphasize the importance of the initial geological situation before fold-and-thrust belt formation.

Modelled nappe-like structures generated from sediments from the half-graben with laterally varying depth show that the nappe geometry strongly depends on the amount of sediments available for nappe formation. The calculation of 3D finite strain shows

630   that the deformation during the formation of nappes originating from the half-graben largely deviates from a 2D plane strain deformation and is of flattening type (Lode's ratio >0). Nappes originating from the laterally homogeneous basin show a more or less laterally straight displacement front indicating that the laterally heterogeneous deformation during nappe formation in the half-graben region does not considerably affect the overthrusting nappe.

The applied strength of the basement has a strong control on the resulting nappe geometry. A relatively stronger basement

635   favors the formation of nappes resembling a thrust nappe while reduced basement strength (modeled by a stress cut-off at 40 MPa) favors the formation of fold nappes.

The initial model configuration was based on geological reconstructions of the Helvetic nappe system. The modelled 3D structures represent a thermo-mechanics based, first-order model for the tectonic evolution of the Helvetic nappe system and show several first-order similarities with this system: (1) Formation of a nappe resulting from the closure of a half-graben.

640   Depending on the model configuration, this nappe can be more similar to a fold or a thrust nappe. The modelled nappes are applicable to the Morcles and Doldenhorn nappes of the Helvetic nappe system. (2) Formation of a laterally homogeneous thrust nappe which overthrusts and is stacked above the underlying nappe resulting from half-graben closure. This nappe is applicable to the Wildhorn and Glarus nappe. (3) The detachment of minor sediment units originally located on the horst and their emplacement between the upper thrust nappe and the underlying nappe from the half-graben. These minor nappes

645   are applicable to the Ardon, Jägerchrütz and Gellihorn nappes. (4) The entrapment of weak sediments, which were originally situated structurally above the sediments eventually forming nappes, between the two major nappes. These entrapped sediments

are applicable to the Ultrahelvetic units. (5) The modelled temperatures, temperature gradients and finite strain gradients are in overall agreement with data from the Helvetic nappe system.

Acknowledgements

References

655 Austin, N., Evans, B., Herwegh, M., and Ebert, A. (2008). Strain localization in the Morcles nappe (Helvetic Alps, switzerland). *swiss Journal of Geosciences*, 101(2):341–360.

Ayrton, S., B. J. B. J. G. Y. and Jemelin, L. (1987). Carte géologique de Chamonix (1/50000). *Orléans: BRGM*.

Ayrton, S. (1980). La géologie de la zone Martigny-Chamonix (versant suisse) et l'origine de la nappe de Morcles (un exemple de subduction continentale).

660 Badertscher, N. P., Abart, R., Burkhard, M., and McCaig, A. (2002). Fluid flow pathways along the Glarus overthrust derived from stable and Sr-isotope patterns. *American Journal of Science*, 302(6):517–547.

Badertscher, N. P. and Burkhard, M. (2000). Brittle–ductile deformation in the Glarus thrust Lochseiten (LK) calc-mylonite. *Terra Nova*, 12(6):281–288.

Bastida, F., Aller, J., Fernandez, F. J., Lisle, R. J., Bobillo Ares, N. C., and Menendez, O. (2014). Recumbent folds: key structural elements
665 in orogenic belts. *Earth-science reviews*, 135:162–183.

Bauville, A. and Schmalholz, S. M. (2013). Thermo-mechanical model for the finite strain gradient in kilometer-scale shear zones. *Geology*, 41(5):567–570.

Bauville, A. and Schmalholz, S. M. (2015). Transition from thin-to thick-skinned tectonics and consequences for nappe formation: Numerical simulations and applications to the Helvetic nappe system, Switzerland. *Tectonophysics*, 665:101–117.

670 Bauville, A. and Schmalholz, S. M. (2017). Tectonic inheritance and kinematic strain localization as trigger for the formation of the Helvetic nappes, Switzerland. *Swiss Journal of Geosciences*, 110(2):523–534.

Bell, T. (1978). Progressive deformation and reorientation of fold axes in a ductile mylonite zone: the Woodroffe thrust. *Tectonophysics*, 44(1-4):285–320.

Bellahsen, N., Jolivet, L., Lacombe, O., Bellanger, M., Boutoux, A., Garcia, S., Mouthereau, F., Le Pourhiet, L., and Gumiaux, C. (2012).
675 Mechanisms of margin inversion in the external Western Alps: Implications for crustal rheology. *Tectonophysics*, 560:62–83.

Bercovici, D. and Ricard, Y. (2003). Energetics of a two-phase model of lithospheric damage, shear localization and plate-boundary formation. *Geophysical Journal International*, 152(3):581–596.

Berger, A., Wehrens, P., Lanari, P., Zwingmann, H., and Herwegh, M. (2017). Microstructures, mineral chemistry and geochronology of white micas along a retrograde evolution: An example from the Aar massif (Central Alps, Switzerland). *Tectonophysics*, 721:179–195.

680 Beutner, E. C. (1977). Causes and consequences of curvature in the Sevier orogenic belt, Utah to Montana.

Boutoux, A., Bellahsen, N., Nanni, U., Pik, R., Verlaguet, A., Rolland, Y., and Lacombe, O. (2016). Thermal and structural evolution of the external Western Alps: Insights from (U–Th–Sm)/He thermochronology and RSCM thermometry in the Aiguilles Rouges/Mont Blanc massifs. *Tectonophysics*, 683:109–123.

Boyer, S. E. and Elliott, D. (1982). Thrust systems. *Aapg Bulletin*, 66(9):1196–1230.

685 Buchanan, J. G. and Buchanan, P. G. (1995). *Basin inversion*, volume 88. Geological Society London.

Bucher, W. H. (1956). Role of gravity in orogenesis. *Geological Society of America Bulletin*, 67(10):1295–1318.

Burkhard, M. (1988). L'Helvétique de la bordure occidentale du massif de l'Aar (évolution tectonique et métamorphique). *Eclogae Geologicae Helvetiae*, 81(1):63–114.

Burkhard, M., Kerrich, R., Maas, R., and Fyfe, W. (1992). Stable and Sr-isotope evidence for fluid advection during thrusting of the Glarus
690 nappe (Swiss Alps). *Contributions to Mineralogy and Petrology*, 112(2-3):293–311.

Butler, R. (1989). The influence of pre-existing basin structure on thrust system evolution in the Western Alps. *Geological Society, London, Special Publications*, 44(1):105–122.

Butler, R. W., Bond, C. E., Cooper, M. A., and Watkins, H. (2019). Fold–thrust structures–where have all the buckles gone? *Geological Society, London, Special Publications*, 487:SP487–7.

Carreras, J., Czeck, D. M., Druguet, E., and Hudleston, P. J. (2010). Structure and development of an anastomosing network of ductile shear zones. *Journal of Structural Geology*, 32(5):656–666.

Casey, M. and Dietrich, D. (1997). Overthrust shear in mountain building. In *Evolution of Geological Structures in Micro-to Macro-scales*, pages 119–142. Springer.

Collet, L. W. (1943). *La nappe de Morcles entre Arve et Rhône*. Kuemmerly und Frey.

Dahlen, F. A. (1984). Noncohesive critical Coulomb wedges: An exact solution. *Journal of Geophysical Research: Solid Earth*, 89(B12):10125–10133.

Dahlen, F. A. and Suppe, J. (1988). Mechanics, growth, and erosion of mountain belts. *Processes in continental lithospheric deformation: Geological Society of America Special Paper*, 218:161–178.

Davis, D., Suppe, J., and Dahlen, F. A. (1983). Mechanics of fold-and-thrust belts and accretionary wedges. *Journal of Geophysical Research*, 88(B2):1153.

Dietrich, D. and Casey, M. (1989). A new tectonic model for the Helvetic nappes. *Geological Society, London, Special Publications*, 45(1):47–63.

Dunn, J. F., Hartshorn, K. G., and Hartshorn, P. W. (1995). Structural styles and hydrocarbon potential of the sub-Andean thrust belt of southern Bolivia.

Ebert, A., Herwegh, M., Berger, A., and Pfiffner, A. (2008). Grain coarsening maps for polymineralic carbonate mylonites: a calibration based on data from different Helvetic nappes (Switzerland). *Tectonophysics*, 457(3-4):128–142.

Ebert, A., Herwegh, M., Evans, B., Pfiffner, A., Austin, N., and Vennemann, T. (2007a). Microfabrics in carbonate mylonites along a large-scale shear zone (Helvetic Alps). *Tectonophysics*, 444(1-4):1–26.

Ebert, A., Herwegh, M., and Pfiffner, A. (2007b). Cooling induced strain localization in carbonate mylonites within a large-scale shear zone (Glarus thrust, Switzerland). *Journal of Structural Geology*, 29(7):1164–1184.

Epard, J. L. (1990). *La nappe de Morcles au sud-ouest du Mont-Blanc*. PhD thesis.

Epard, J.-L. and Escher, A. (1996). Transition from basement to cover: a geometric model. *Journal of Structural Geology*, 18(5):533–548.

Epard, J.-L. and Groshong Jr, R. H. (1993). Excess area and depth to detachment. *AAPG bulletin*, 77(8):1291–1302.

Escher, A., Masson, H., and Steck, A. (1993). Nappe geometry in the western Swiss Alps. *Journal of structural Geology*, 15(3-5):501–509.

Fernandez, N. and Kaus, B. J. (2014). Fold interaction and wavelength selection in 3D models of multilayer detachment folding. *Tectonophysics*, 632:199–217.

Fitz Diaz, E., Hudleston, P., and Tolson, G. (2011). Comparison of tectonic styles in the Mexican and Canadian Rocky Mountain fold-thrust belt. *Geological Society, London, Special Publications*, 349(1):149–167.

Gillcrist, R., Coward, M., and Mugnier, J.-L. (1987). Structural inversion and its controls: examples from the Alpine foreland and the French Alps. *Geodinamica acta*, 1(1):5–34.

Granado, P. and Ruh, J. B. (2019). Numerical modelling of inversion tectonics in fold-and-thrust belts. *Tectonophysics*, 763:14–29.

Hamilton, W. B. (1988). Laramide crustal shortening. *Interaction of the Rocky Mountain foreland and the Cordilleran thrust belt: Geological Society of America Memoir*, 171:27–39.

Hansen, F., Carter, N., et al. (1983). Semibrittle creep of dry and wet Westerly granite at 1000 MPa. In *The 24th US Symposium on Rock Mechanics (USRMS)*. American Rock Mechanics Association.

Herwegh, M., Berger, A., Baumberger, R., Wehrens, P., and Kissling, E. (2017). Large-scale crustal-block-extrusion during late Alpine collision. *Scientific reports*, 7(1):413.

Herwegh, M., HüRZELER, J.-P., Pfiffner, O. A., Schmid, S. M., Abart, R., and Ebert, A. (2008). the Glarus thrust: excursion guide and report of a field trip of the swiss tectonic studies Group (swiss Geological society, 14.–16. 09. 2006). *swiss Journal of Geosciences*, 101(2):323–340.

Herwegh, M. and Pfiffner, O.-A. (2005). Tectono-metamorphic evolution of a nappe stack: A case study of the Swiss Alps. *Tectonophysics*, 404(1-2):55–76.

Hürzeler, J.-P. and Abart, R. (2008). Fluid flow and rock alteration along the Glarus thrust. *swiss Journal of Geosciences*, 101(2):251–268.

Jaquet, Y., Bauville, A., and Schmalholz, S. M. (2014). Viscous overthrusting versus folding: 2-D quantitative modeling and its application to the Helvetic and Jura fold and thrust belts. *Journal of Structural Geology*, 62:25–37.

Jaquet, Y., Duretz, T., Grujic, D., Masson, H., and Schmalholz, S. M. (2018). Formation of orogenic wedges and crustal shear zones by thermal softening, associated topographic evolution and application to natural orogens. *Tectonophysics*, 746:512–529.

Jaquet, Y., Duretz, T., and Schmalholz, S. M. (2015). Dramatic effect of elasticity on thermal softening and strain localization during lithospheric shortening. *Geophysical Journal International*, 204(2):780–784.

Kaus, B., Popov, A. A., Baumann, T., Pusok, A., Bauville, A., Fernandez, N., and Collignon, M. (2016). Forward and inverse modelling of lithospheric deformation on geological timescales. In *Proceedings of NIC Symposium*.

Kirschner, D., Masson, H., and Sharp, Z. (1999). Fluid migration through thrust faults in the Helvetic nappes (Western Swiss Alps). *Contributions to Mineralogy and Petrology*, 136(1-2):169–183.

Kirschner, D. L., Cosca, M. A., Masson, H., and Hunziker, J. C. (1996). Staircase 40/Ar39Ar spectra of fine-grained white mica: Timing and duration of deformation and empirical constraints on argon diffusion. *Geology*, 24(8):747–750.

Kirschner, D. L., Sharp, Z. D., and Masson, H. (1995). Oxygen isotope thermometry of quartz-calcite veins: Unraveling the thermal-tectonic history of the subgreenschist facies Morcles nappe (Swiss Alps). *Geological society of America bulletin*, 107(10):1145–1156.

Kiss, D., Podladchikov, Y., Duretz, T., and Schmalholz, S. M. (2019). Spontaneous generation of ductile shear zones by thermal softening: Localization criterion, 1D to 3D modelling and application to the lithosphere. *Earth and Planetary Science Letters*, 519:284–296.

Kronenberg, A. K., Kirby, S. H., and Pinkston, J. (1990). Basal slip and mechanical anisotropy of biotite. *Journal of Geophysical Research: Solid Earth*, 95(B12):19257–19278.

Lacombe, O. and Bellahsen, N. (2016). Thick-skinned tectonics and basement-involved fold–thrust belts: insights from selected Cenozoic orogens. *Geological Magazine*, 153(5-6):763–810.

Lacombe, O. and Mouthereau, F. (2002). Basement-involved shortening and deep detachment tectonics in forelands of orogens: Insights from recent collision belts (Taiwan, Western Alps, Pyrenees). *Tectonics*, 21(4):12–1.

Laubscher, H. (1972). Some overall aspects of Jura dynamics. *American Journal of Science*, 272(4):293–304.

Leloup, P.-H., Arnaud, N., Sobel, E. R., and Lacassin, R. (2005). Alpine thermal and structural evolution of the highest external crystalline massif: The Mont Blanc. *Tectonics*, 24(4).

Lode, W. (1926). Versuche über den Einfluß der mittleren Hauptspannung auf das Fließen der Metalle Eisen, Kupfer und Nickel. *Zeitschrift für Physik*, 36(11-12):913–939.

Lymer, G., Cresswell, D. J., Reston, T. J., Bull, J. M., Sawyer, D. S., Morgan, J. K., Stevenson, C., Causer, A., Minshull, T. A., and Shillington, D. J. (2019). 3D development of detachment faulting during continental breakup. *Earth and Planetary Science Letters*, 515:90–99.

Macedo, J. and Marshak, S. (1999). Controls on the geometry of fold-thrust belt salients. *Geological Society of America Bulletin*, 111(12):1808–1822.

770   Mair, D., Lechmann, A., Herwegh, M., Nibourel, L., and Schlunegger, F. (2018). Linking Alpine deformation in the Aar Massif basement and its cover units–the case of the Jungfrau–Eiger mountains (Central Alps, Switzerland). *Solid Earth*, 9:1099–1122.

Marshak, S., Wilkerson, M., and Hsui, A. (1992). Generation of curved fold-thrust belts: Insight from simple physical and analytical models. In *Thrust tectonics*, pages 83–92. Springer.

Mase, G. E. (1970). *Continuum mechanics*, volume 970. McGraw-Hill New York.

775   Masson, H., Baud, A., Escher, A., Gabus, J., and Marthaler, M. (1980). Paléokarsts crétacés et tertiaires dans la nappe de Morcles. *Compte rendu de l'excursion de la Société géologique Suisse du*, 1:331–349.

Milnes, A. G. and Pfiffner, O.-A. (1980). Tectonic evolution of the Central Alps in the cross section St. Gallen-Como. *Eclogae Geologicae Helvetiae*, 73(2):619–633.

Mitra, G. (1997). Evolution of salients in a fold-and-thrust belt: the effects of sedimentary basin geometry, strain distribution and critical

780   taper. In *Evolution of geological structures in micro-to macro-scales*, pages 59–90. Springer.

Mitra, S. and Fisher, G. W. (1992). *Structural geology of fold and thrust belts*. Johns Hopkins University Press.

Mouthereau, F., Deffontaines, B., Lacombe, O., Angelier, J., Byrne, T., and Liu, C. (2002). Variations along the strike of the Taiwan thrust belt: Basement control on structural style, wedge geometry, and kinematics. *Special Papers-Geological Society of America*, pages 31–54.

Nádai, A. and Hodge, P. (1963). Theory of Flow and Fracture of Solids, vol. II. *Journal of Applied Mechanics*, 30:640.

785   Nemčok, M., Mora, A., and Cosgrove, J. (2013). Thick-skin-dominated orogens; from initial inversion to full accretion: an introduction. *Geological Society, London, Special Publications*, 377(1):1–17.

Nibourel, L., Berger, A., Egli, D., Luensdorf, N. K., and Herwegh, M. (2018). Large vertical displacements of a crystalline massif recorded by Raman thermometry. *Geology*, 46(10):879–882.

Oulianoff, N. (1924). *Le massif de l'Arpille et ses abords: avec 11 figures dans le texte, 2 planches et une carte géologique au 1: 25000 (no.

790   103)*. Francke.

Paréjas, E. (1922). *Géologie de la zone de Chamonix, comprise entre le Mont-Blanc et les Aiguilles Rouges*.

Peña, J. M. V. and Catalán, J. R. M. (2004). A computer program for the simulation of folds of different sizes under the influence of gravity. *Computers & geosciences*, 30(1):33–43.

Pfiffner, O. A. (1993). The structure of the Helvetic nappes and its relation to the mechanical stratigraphy. *Journal of structural Geology*,

795   15(3-5):511–521.

Pfiffner, O. A. (2006). Thick-skinned and thin-skinned styles of continental contraction. *Special Papers-Geological Society of America*, 414:153.

Pfiffner, O. A. (2015). *Geologie der Alpen*, volume 8416. UTB.

Pfiffner, O.-A., Burkhard, M., Hänni, R., Kammer, A., Kligfield, R., Mancktelow, N., Menkveld, J., Ramsay, J., Schmid, S., and Zurbriggen,

800   R. (2011). Structural map of the Helvetic zone of the Swiss Alps, including Vorarlberg (Austria) and Haute Savoie (France).

Poulet, T., Veveakis, M., Herwegh, M., Buckingham, T., and Regenauer Lieb, K. (2014). Modeling episodic fluid-release events in the ductile carbonates of the Glarus thrust. *Geophysical Research Letters*, 41(20):7121–7128.

Price, N. J. and McClay, K. R. (1981). Thrust and nappe tectonics. Geological Society of London.

Ramsay, J. (1981). Tectonics of the Helvetic nappes. *Geological Society, London, Special Publications*, 9(1):293–309.

805 Ramsay, J. (1989). Fold and fault geometry in the western Helvetic nappes of Switzerland and France and its implication for the evolution of the arc of the western Alps. *Geological Society, London, Special Publications*, 45(1):33–45.

Ramsay, J. G., Casey, M., and Kligfield, R. (1983). Role of shear in development of the Helvetic fold-thrust belt of Switzerland. *Geology*, 11(8):439–442.

Ramsay, J. G. and Huber, M. I. (1987). *The techniques of modern structural geology: Folds and fractures*, volume 2. Academic press.

810 Ries, A. (1976). A Discussion on natural strain and geological structure-Patterns of strain variation in arcuate fold bets. *Philosophical Transactions of the Royal Society of London. Series A, Mathematical and Physical Sciences*, 283(1312):281–288.

Rodgers, J. (1949). Evolution of thought on structure of middle and southern Appalachians. *AAPG Bulletin*, 33(10):1643–1654.

Ruh, J. B., Gerya, T., and Burg, J.-P. (2014). 3D effects of strain vs. velocity weakening on deformation patterns in accretionary wedges. *Tectonophysics*, 615:122–141.

815 Ruh, J. B., Kaus, B. J., and Burg, J.-P. (2012). Numerical investigation of deformation mechanics in fold-and-thrust belts: Influence of rheology of single and multiple décollements. *Tectonics*, 31(3).

Schmalholz, S., Podladchikov, Y., and Burg, J.-P. (2002). Control of folding by gravity and matrix thickness: Implications for large-scale folding. *Journal of Geophysical Research: Solid Earth*, 107(B1):ETG–1.

Schmid, S., Boland, J., and Paterson, M. (1977). Superplastic flow in finegrained limestone. *Tectonophysics*, 43(3-4):257–291.

820 Schmid, S. M. (1975). The Glarus overthrust: Field evidence and mechanical model. *Ecologae Geol. Helvetia*, 68:247–280.

Simpson, G. (2011). Mechanics of non-critical fold-thrust belts based on finite element models. *Tectonophysics*, 499(1-4):142–155.

Steck, A. (1999). *Carte tectonique des Alpes de Suisse occidentale et des régions avoisinantes*. Office fédéral des eaux et de la géologie.

Termier, P. (1906). *La synthèse géologique des Alpes*.

Thomas, W. A. (1977). Evolution of Appalachian-Ouachita salients and recesses from reentrants and promontories in the continental margin.

825 *American Journal of Science*, 277(10):1233–1278.

Trümpy, R., Aubert, D., and Bernoulli, D. (1980). *Geology of Switzerland: Geological excursions*, volume 10. Wepf.

Von Tscharner, M., Schmalholz, S., and Epard, J.-L. (2016). 3-D numerical models of viscous flow applied to fold nappes and the Rawil depression in the Helvetic nappe system (western Switzerland). *Journal of Structural Geology*, 86:32–46.

Wehrens, P., Baumberger, R., Berger, A., and Herwegh, M. (2017). How is strain localized in a meta-granitoid, mid-crustal basement section?

830 Spatial distribution of deformation in the central Aar massif (Switzerland). *Journal of structural geology*, 94:47–67.

Wissing, S. and Pfiffner, O.-A. (2003). Numerical models for the control of inherited basin geometries on structures and emplacement of the Klippen nappe (Swiss Prealps). *Journal of structural geology*, 25(8):1213–1227.

Yamato, P., Kaus, B. J., Mouthereau, F., and Castelltort, S. (2011). Dynamic constraints on the crustal-scale rheology of the Zagros fold belt, Iran. *Geology*, 39(9):815–818.